Multi-wavelength characterization of the Very High Energy blazar OT 081

Ana Esteban Gutiérrez

Tutorized by : Josefa Becerra González & Ramón García López

July, 2018

• University of La Laguna. Science Faculty, Physics Section •

- Department of Astrophysics -

Resumen

La astronomía de rayos gamma de muy alta energía (VHE, E > 100 GeV) comenzó hace muy poco tiempo, detectándose la primera fuente de VHE hace tan solo 28 años. Desde entonces, la astronomía de VHE solo se ha desarrollado como experimentos con sensibilidad limitada (ahora en construcción el primer observatorio para VHE, CTA). Dado que la atmósfera terrestre es opaca a este tipo de radiación, ha sido necesario el estudio de estos rayos gamma en altas energías (HE, 100 MeV < E < 100 GeV) con satélites desde el espacio, así como el desarrollo de técnicas de detección indirectas basadas en el efecto Cherenkov para la detección desde tierra de estos rayos gamma en VHE. A este tipo de telescopios se les llama telescopios tipo Cherenkov o IACTs por sus siglas en inglés, Imaging Atmospheric Cherenkov Telescope, siendo los que tenemos en la actualidad de últimas generaciones los llamados MAGIC, HESS y VERITAS.

El cielo en el rango de VHE todavía se encuentra muy inexplorado, estando el cielo extragaláctico de VHE compuesto solo de 72 objetos (66 de ellos son blazars) y la mayoría de ellos solo detectables durante los estados alta emisión o flares. Por lo tanto, en el dominio de rayos gamma de VHE todavía estamos en la fase de descubrimiento, de modo que el estudio de cada fuente individual es importante. En concreto, el blazar OT081 o también llamado PKS 1749+096, fue seleccionado como un buen candidato VHE basado en sus características de longitud de onda múltiple. Fue detectado en rayos gamma de VHE en 2016 con los telescopios MAGIC durante un flare que observó el satelite Fermi-LAT. También fue observado en rayos X por el satélite Swift. Del mismo modo se observa una posible correlación con el óptico al detectarse este mismo flare en la banda del visible.

Los blazars son un tipo de Núcleo Activo de Galaxía en el que hay presencia de jets y que se caracteriza porque el eje de dicho jet está apuntando en la misma dirección que nuestra línea de visión. Este tipo de AGN (Active Galactic Nucleus, por sus siglas en inglés) son muy útiles a la hora de estudiar la emisión en el jet y cómo se están generando los rayos gamma que luego detectamos en tierra con IACTs y en el espacio con satélites. Típicamente se ha visto que los blazars emiten en todas las frecuencias (desde radio hasta rayos gamma) aunque el radio se cree que se localiza en las partes más externas del jet, separado del resto de bandas de energía que se situarían en partes más internas. Esta emisión del jet que se visualiza en la SED (Spectral Energy Distribution, por sus siglas en inglés) se puede modelar teniendo en cuenta varios procesos acordes a dos tipos de escenarios distintos: el leptónico y el hadrónico (o la combinacion de ambos, denominado lepto-hadronicos). Esta distinción se hace básicamente para explicar el origen de la emisión de más alta energía, siendo la de más baja energía ya establecida y producida por radiación tipo Synchrotron.

En este trabajo, se realizará un análisis detallado de los datos de MAGIC. También analizaremos las observaciones de rayos gamma de alta energía del instrumento LAT a bordo del satélite de rayos gamma Fermi. La emisión de rayos gamma se estudiará en el contexto de las observaciones multi-frecuencia desde la banda de radio hasta los rayos gamma. Por último, analizaremos las propiedades de la distribución espectral de energía y probaremos el escenario teórico Synchrotron Self-Compton (SSC) para estas observaciones. El esquema detallado de lo que se incluye en cada sección de este trabajo se muestra a continuación:

- La Sección 1 muestra una introducción de la astrofísica de rayos gamma y sus procesos de producción, focalizandose en la física de los AGNs y los distintos modelos que abordan la emisión de los jets junto con la absorción que se produce desde que esta radiación se emite en la fuente hasta que llega a nuestros detectores. Asímismo, explica en qué se basa la técnica de detección indirecta de estos rayos gamma desde tierra por el efecto Cherenkov y una breve descripción de los telescopios con los que se han tomado los datos y sus características principales, tanto de Fermi en el rango HE como de MAGIC a VHE.

- La Sección 2 detalla las motivaciones y objetivos principales de este trabajo y un resumen de los estudios que se han publicado acerca de nuestra fuente.

- La Sección 3 expone los dos tipos de análisis de datos realizados de nuestra fuente, tanto para los telescopios MAGIC como para el satélite Fermi. Explica de forma detallada las rutinas utilizadas dentro de cada software y los pasos realizados para poder obtener las curvas de luz y las distribuciones espectrales de energía durante el período de tiempo que dura el estallido o flare.

- La Sección 4 describe los resultados obtenidos a partir de los dos análisis previos junto con datos de otras frecuencias (desde radio hasta rayos X). A partir de esas medidas y de la construcción de una curva de luz y una distribución espectral de energía, ambas en multi-frecuencia, se discuten las características del flare y cómo ha variado el flujo respecto al estado de reposo (low state) de nuestra fuente. En el caso de la distribución espectral de energía en multi-frecuencia, se explora la variabilidad en la clasificación del tipo de blazar para nuestra fuente a través de la proporción entre la emisión de más alta energía con respecto a la de más baja energía. Además, en esta sección se incluye el modelado a la emisión del jet a partir de nuestros datos escogiendo el escenario de Synchrotron Self-Compton (SSC), obteniendo así varios de los parámetros físicos que describen la emisión. Finalmente se compara el ajuste de este modelo con los resultados de otra fuente del mismo tipo que la nuestra, a la que los autores de ese estudio también han aplicado un modelo SSC.

- La Sección 5 presenta las conclusiones extraídas de ambos análisis y de los estudios realizados, además de las mejoras en el ajuste al modelo SSC que se podrían aplicar para continuar con estudio del blazar OT 081.

- La Sección 6 finaliza con las perspectivas futuras que se esperan de cara a la astrofísica de rayos gamma y el estudio de estas fuentes desde tierra con las nuevas generaciones de telescopios tipo Cherenkov.

- Este trabajo también cuenta con un apéndice gráfico donde se recoge una figura de mayor tamaño para una mejor visualización de la misma, así como los agradecimientos y una bibliografía donde se encuentran enumeradas todas las referencias a los artículos, páginas web y recursos que han sido consultadas.

Contents

1 Introduction theory

The Electromagnetic Spectrum covers a wide range of energies from extremely low energies of radio waves to the highest energies ever reached of the order of TeV. This most energetic radiation is known as gamma rays and the Earth's atmosphere is not transparent to these photons. Due to this fact, satellites were put in the space orbiting our planet to be able to measure the γ rays. Nevertheless, only High Energy (HE, E > 100 MeV) γ rays can be measured. For the Very High Energy (VHE, E > 100 GeV) γ rays, observations from space are not feasible as the fluxes at such energies are too faint, therefore, we would need bigger instrumentation with huge collective areas and that means heavier telescopes which are not possible to launch into orbit becasuse of the weight. To solve this problem, new indirect techniques for ground detection were developed around three decades ago, which consists of having detectors for the measurement of Cherenkov cascades which are produced in the atmosphere. When a γ ray reaches the Earth's atmosphere, a shower of particles is produced due to the interaction. At that point, these secondary particles start to travel across it at speeds greater than light in that environment emitting Cherenkov radiation, so that the Earth's atmosphere acts as a calorimeter.

In this chapter, a short introduction to the world of HE and VHE γ rays will be presented, focusing on Active Galactic Nuclei (AGNs) sources and the techniques that allow us to have information about the responsible emission processes. In addition, a brief description of the γ-ray telescopes used for this study will be given.

1.1 VHE Astrophysics

The VHE range covers approximately E > 100 GeV and involves the most energetic processes inside and outside our Galaxy. The Earth is continously bombarded by Cosmic Rays (CRs), which are mostly composed by protons (87%), α particles (11%), electrons and positrons (2%), ionized nuclei of C, N, O and Fe (1%), neutrons, neutrinos and a small fraction of γ rays. The origin of these CRs is unknown, so the study of the γ rays is helping to find more information about the CRs. Some parts of interest in the spectrum of the CRs are shown in Figure 1. In this way, they can provide us a hint about the nature of these particles that reach the Earth's atmosphere.

The energy spectrum of the CRs goes from $\sim 10^8$ to $\sim 3 \cdot 10^{20}$ eV and it is well fitted to a power law of the type: $F \sim E^{-\Gamma}$ characterised by non-thermal processes (see Figure 1). There are two changes in the spectral index of the power law called the 'knee' and the 'anckle'. The first one is at E $\sim 5 \cdot 10^{15}$ eV and the second one is at E$\sim 3 \cdot 10^{18}$ eV and between these two features, the spectral index is $\sim$3. However, below the 'knee' (lower energies) and above the 'anckle' (higher energies) the index changes to $\sim$2.7. It is thought that CRs reaching the Earth up to the 'knee' have a Galactic origin and the other ones above the 'anckle' are extragalactic, but the main debate nowadays is the genesis of the CRs between these two features in the spectrum. In addition, the origin of the highest part of the spectrum called ultra-high energetic CRs is also still unknown.
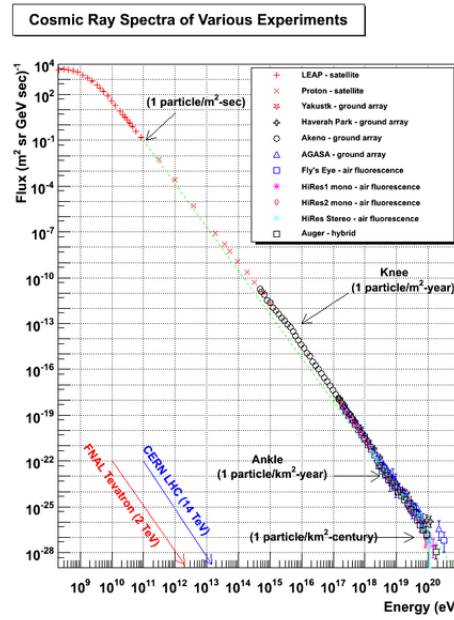
Fig 1. Cosmic Ray spectrum plotted with data from several experiments. Retrieved from:
http://www.physics.utah.edu/~whanlon/spectrum.html

The CRs are charged particles and can interact with the magnetic fields, and therefore, they are deviated from their original trajectory when they travel across the Universe. The γ rays are the most energetic photons produced by these charged particles via different mechanisms. Since they are neutrally charged, they do not suffer from deviations and point directly to their progenitors. So γ rays can help us to find places which are most likely responsible for the acceleration of CRs. Because of that, the study of these γ rays can provide us information about the source where they are coming and the mechanisms involved, as well as the particularities of the interstellar/intergalactic medium that they have crossed until reaching our telescopes.

1.2   The γ-ray processes

There are mainly two types of theoretical scenarios to explain the production of γ rays: leptonic and hadronic scenario, and a combination of both, called lepto-hadronic models.

On the one hand, within the leptonic scenario there are three mechanisms involved that are able to explain the production of these high energy photons: Bremsstrahlung, Inverse Compton (IC) and Synchrotron radiation.

- Bremsstrahlung: This emission is originated when an electron passes near a charged particle and it is decelerated and deflected due to the effect of the electrostatic field of this charged particle. The radiation produced covers the range of the X-rays and up to low energy γ rays ($\sim$ 100 MeV).

- Inverse Compton (IC): The emission is produced due to the interaction of a low energy photon and an energetic electron (relativistic). Due to the scattering of the photon by the electron, there

is a transfer of energy from the electron to the photon. This low energy photon can be boosted up to the VHE band. It can be distinguished two regimes depending on the energies of the two particles involved: $E_\gamma \cdot E_{e^-} << me^2c^4$,where the scattering would be within the Thomson regime (σ_T) and the spectral index of the energy power law results: $(\Gamma+1)/2$, on the contrary, if $E_\gamma \cdot E_{e^-} >> me^2c^4$, then the Klein-Nishina (KN) regime is applied changing the spectral index to $(\Gamma+1)$.

- Synchrotron: This emission type is originated by charged particles travelling fast within a magnetic field and producing photons with typically lower energies up to X-rays. In some cases, the γ-ray emission can also be produced when there are involved ultra-high CRs and/or strong magnetic fields.

On the other hand, within the hadronic scenario the π^0 decay mechanism is able to explain the origin of γ rays: π^0 can decay in a pair of γ photons ($\pi^0 \rightarrow \gamma + \gamma$). Its lifetime is very short and tipically decays before interacting with the medium.
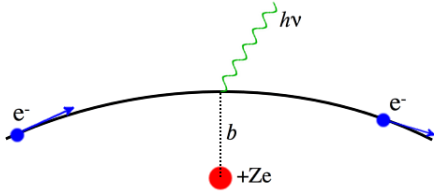

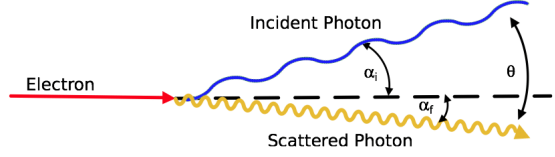**Fig 2.** Sketch of the Bremsstrahlung emission .

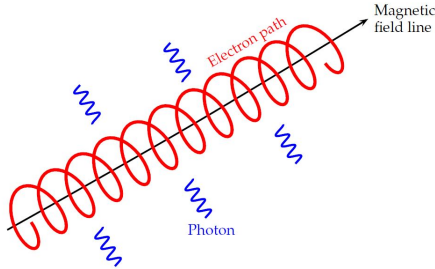**Fig 3.** Sketch of the Inverse Compton emission.

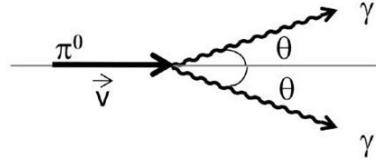**Fig 4.** Sketch of the Synchrotron emission.

Fig 5. Sketch of the π^0 decay emission.

As we are interested in the study of VHE γ rays, we briefly discuss the possible production places in the Universe. The VHE γ-ray production can take place at different sources either from galactic or extragalactic nature: in the first group there are included Compact Binary Systems, the Galactic center (with its Supermassive black hole Sgr A*), Supernovae Remnants (they could be the accelerators of galactic type CRs), Pulsars and Pulsar Wind Nebulae. The exragalactic VHE emitters are: Active Galactic Nuclei (AGNs) which are basically galaxies hosting a Supermassive Black Hole in their centers (further information will be detailed in section 1.3 because it is the kind of source we are treating during this work). In addition, Gamma Ray Bursts or GRBs (short and intense γ-ray emission) are being searched but no detection has been achieved yet.

1.3 AGNs

We call AGNs to the galaxies which centers emit more radiation than the rest of the structure. This excess in luminosity has been observed in almost all the multi-wavelength range of the electromagnetic spectrum and it is already known that its origin is not caused by the emission of the stars in the galaxy. It is believed that it could be a result of a Supermassive Black Hole accreting mass at the center of the host galaxy. Furthermore, some of these AGNs host jets which usually present variability in the flux, revealed as 'flares', that can last from minutes to months.

Within the Unified Model, AGNs can be divided into different types depending on the orientation we are looking at the host galaxy, called the viewing angle. Moreover, intrinsic features in their spectra associated to different physical processes can be seen according to the previous classification.
As we can see in Figure 6, radio-quiet AGNs are typically hosted by spiral/irregular galaxies or Quasars (QSOs) and we call Seyfert 1 or Seyfert 2 to those AGNs without the presence of jets. The first subtype shows broad and narrow lines in the spectrum while the second one only has narrow lines.
Meanwhile, radio-loud AGNs do actually have jets and there are two types: FR and blazars. In the Faranoff-Riley galaxies (FR), we find two subgroups: FRI and FRII, which are mainly distinguished by a lower or a higher luminosity in the AGN. In this case, the jet is positioned with a certain angle with respect to our line of sight. Meanwhile, the blazars are typically those compact sources that appear when we are looking in the direction of the jets. Beacause of these jets are too energetic, they shield a large part of the emission coming from the other parts of the AGN. Besides, their emission is boosted due to relativistic effects caused by geometrical effects. This is the class we are interested in because they are powerful γ-ray emitters which dominates the γ-ray sky.
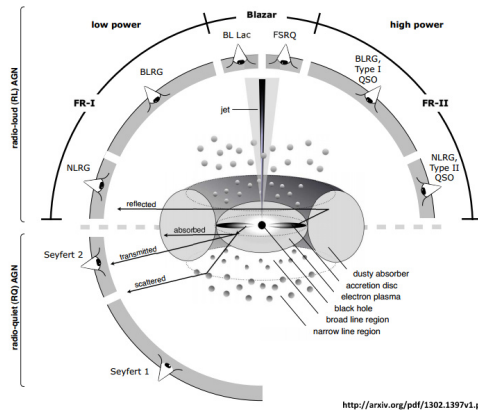

Fig 6. AGN Unified Model (Beckmann and Shrader, 2012)

The typical structure of an AGN is also shown in Figure 6. The different components from the center towards the outer regions are listed, starting with the Black Hole and its rotating accretion disk that emits thermal emission, a very hot population of electrons surrounding the disk called corona, the broad line region (BLR) at a distance of $\sim$ 0.1-1 pc, the torus of dust and gas located at $\sim$1-10 pc, the narrow line region (NLR) situated at $\sim$100 pc and finally the jets (only appear in the case of radio-loud AGNs) which are quite collimated, symmetric and perpendicular to the accretion disk plane and they can reach distances over $\sim$100 kpc from the center. Actually, these jets are not only external but they

born very close to the Black Hole. They radiate from radio to VHE γ rays, being the only part of the AGN capable to emit γ rays.

Blazars emit through the entire Electromagnetic Spectrum, from radio to the VHE band. The Spectral Energy Distributions (SEDs) show a doubled-peaked structure with the first bump between the range of radio to optical or X-rays (depending on the blazar type) and the second bump located at the highest energy range (from MeV to GeV). The lower energy bump is originated by the Synchrotron radiation inside the jet. However, the origin of the higher energy bump is still under debate. In order to explain it, there are some theoretical scenarios that can model the jet emission, which will be given in subsection 1.3.1.

The different types of blazars can be properly classified according to the shape of their SEDs. *The blazar sequence* is a distribution that shows the main differences between these sources, taking into account the peak frequencies of the two bumps, the integral flux and the radio emission. Systematic studies of recent discoveries were performed for that purpose, giving as a result the most recent published plot of this kind (see Figure 7).
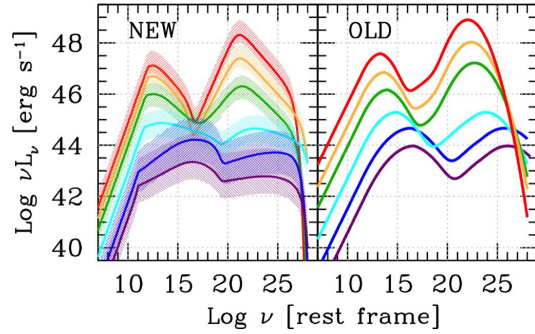

Fig 7. A comparison between the new and the original blazar sequence (G. Ghisellini et al., 2017). Different color lines represent the various types of blazar. The red line represents the FSRQs, while the rest of the lines represents BL Lac objects: the yellow line for LBLs, the green line for IBLs and the light blue, dark blue and purple lines for HBLs.

Blazars can be subdivided in two classes: Flat Spectrum Radio Quasars (FSRQs) and BL Lac objects. The main differences between them lay on: the optical spectrum, the SED peak positions and the Compton dominance (relation between the first and the second peak of their SEDs).

FSRQs exhibit a flat spectrum with broad optical emission lines and BL Lac objects are mainly dominated by the continuum from the jet and display very weak narrow optical emission lines (if any). Depending on the frequency of the first peak in their SEDs, BL Lacs objects are classified in three different subtypes: low peaked (LBL; $\nu_1 < 10^{14}\,Hz$), intermediate peaked (IBL; $10^{14} \leq \nu_1 < 10^{15}\,Hz$) and high peaked (HBL; $\nu_1 \geq 10^{15}\,Hz$). The first peak coverage depends on the source type. For FSRQs and low energy peaking BL Lac objects, the first SED peak goes from radio to optical-UV. But for high energy peaking it also includes X-rays (see the blazar sequence in Figure 7). The majority of the observed BL Lacs in the VHE band are classified as HBLs, since from the LBL subtype and FSRQs it is harder to detect them. This is because the spectrum at the VHE band is already pretty steep, and presents low fluxes so they are typically detected only during high states.

The Compton dominance is referred to the comparison between the luminosity of the second peak with respect to the first peak in the SEDs. As shown in Figure 7, in the case of FSRQs (red line),

the difference between the bumps is much higher than the case of BL Lac objects (rest of the lines) and it is linked with the physical processes involved in the jet. It can be also seen that this Compton dominance changes between the different subclasses of BL Lac objects, as it is higher for LBLs (yellow line) than for HBLs (from light blue to purple lines).

1.3.1   Jet emission models

Up to now, the information of the jets formation is still unkown, but some studies indicate that their origin may come from the accretion disk region, near to the center of the AGN. Besides, their emission processes are thought to be caused by electrically charged particles moving at relativistic velocities along these jets, where magnetic fields are also present. Therefore, some measured quantities as the observed time or the frequency will be affected by the so called beaming effect, due to the high velocities of the particles inside the jets.

As we already seen, there are two bumps in the blazar SEDs. Low energy is due to Synchrotron of electrons while the high energy bump can be explained by two main scenarios according to the nature of the emitting particle: the leptonic model or the hadronic model. The interaction in the leptonic model is performed by electrons (or positrons) and photons, while in the hadronic model the involved particle could be the proton and its possible interaction with other particles and photons, and/or the π^0 particle.

Within the leptonic models, the high energy radiation is originated by Inverse Compton (IC) scattering. Three different types of IC can be identified to explain this emission:

- Synchrotron-Self Compton (SSC): In this particular case, the IC scattering is originated from those synchrotron photons previously emitted in the jet by the same population of electrons. This second process of Compton scattering can occur in both Thomson or KN regimes, depending on the energy of the electrons in the jet. The VHE emission typically occurs in the KN regime.

- External Compton (EC): This jet emission appears when there is an injection of photons that come from any of the external photon fields present in the AGN: the optical-UV emission coming from the BLR and/or the infrared radiation produced by the torus.

- The Mirror model: Within this specific case, the reflection of some part of the synchrotron radiation by the BLR of the AGN is taken into account when this emission travels back to the jet, interacting with the electrons in the jet. However, this effect does not have a gret contribution to the jet emission.

Otherwise, the Hadronic models consider that the emission of the jet at lower frequencies is due to Synchrotron radiation originated by relativistic electrons but at higher frequencies, the involved

particles are the protons or π^0 inside the jet. The hadronic processes are usually slower than the leptonic ones, so it becomes difficult to explain the characteristic variability of the AGNs with this type of models. However, this model still presents an interesting alternative for some particular cases, as for example the blazars where neutrinos are expected.

In addition, it exists a third possibility for the jet emission at VHE defined as a mixture between the hadronic and the leptonic models, called The lepto-hadronic model. Within this new category, both processes contribute significantly to the high energy bump.

1.3.2   γ-ray absorption

The absorption of γ-ray photons can take place inside or outside the source of study. Self-absorption takes place inside the AGN via pair production mechanisms. In addition, different components of intergalactic background radiation are affecting as well to those γ-ray photons until they reach the Earth's atmosphere.

The self-absorption process depends on the energy of the target photons because it requires a certain energy range to reach the energy threshold for pair creation. Therefore, this effect changes in terms of the emission zone location within the AGN structure. If the emitting region within the jet is located close to the central engine within the BLR, the γ rays can interact via pair production with the UV/optical photons and be absorbed. If the emitting region is instead located farther away, the absoption will occur due to the interaction with the IR photons created by the dust torus. However, in case of BL Lac objects there are no evidences for strong BLR and/or dust torus. Therefore, BL Lac objects are typically free of self-absorption.

With respect to the background radiation, it is composed not only by the diffuse sources but also by the radiation originated in different energy bands, as it can be the very well known CMB. In Figure 8 it can be seen the influence of different types of background radiation accroding to the frequencies of the target photons. The main contribution to the absorption is from the Microwaves (CMB), however, due to its high flux it will only affect to those photons with energies $\gtrsim$ 80 TeV. Meanwhile, the second main contribution to take into account is given by the Optical and Infrared ranges, also known by the name of Extragalactic Background Light (EBL). This two peak structure that EBL presents is caused by the starlight and its re-emission by dust, in optical and infrared respectively.
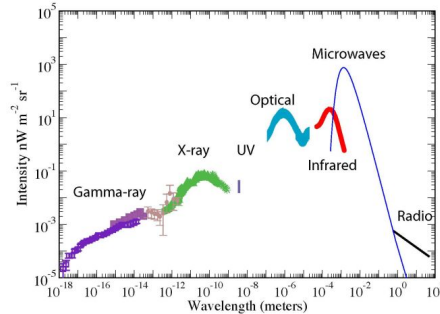

Fig 8. Intensity of all the background radiation components as a function of the wavelength (Cooray A., 2016).

Because of the absorption produced by the background radiation, the intrinsic flux (F_{int}) of a source is actually distorted and different from which we receive, the observed flux (F_{obs}). The difference is an exponential decay given by the optical depth (τ), as it can be seen in the Equation (1)
.

$$F_{obs}(E) = F_{int}(E) \cdot e^{-\tau(E,z)} \tag{1}$$

This optical depth depends on the energy range and the redshift of the source. As the spectrum of the AGNs typically covers from few tens of GeV to few TeV, the SED would just be affected by the EBL absorption. In addition, it is clear that the longer the photons travel, the higher is the probability of interaction, so it is also needed to know the distance (redshift) to our source.

EBL models
Then, we need to perform an EBL-correction to be able to calculate the de-absorbed spectra and obtain the intrinsic fluxes. Nevertheless, the estimation of this EBL results a difficult task, since it depends on the evolution of the Universe and the foregrounds shield the background contribution. For this reason, there are some EBL models that try to fit as well as possible the two characterictic bumps of this absorption. They are based on direct and indirect methods and can be divided into these three following groups:

- Forward evolution: it is based on galaxy evolution and it assumes some stellar evolution models to simulate how the Universe evolves since the birth of the first stars (Kneiske and Dole, 2010).

- Backward evolution: it is the same as the previous one, but starting with the present Universe and developing it back in time. It uses observations of local galaxies and extrapolate the results to higher redshifts. Average templates from observed SEDs are applied for the stellar emission. (Franceschini et al., 2008).

- Observed galaxy evolution: this model uses data from direct observations of galaxies to extrapolate their evolution. (Domínguez et al., 2011).

These three models are in good agreement even though they do not work with the same assumptions. However, these approaches are still not perfect and uncertainties of the order of 2-3 are present in EBL models.

1.4 VHE γ-ray detection: The Imaging Atmospheric Cherenkov Telescope (IACT) Technique

The space-based experiments can observe directly HE γ rays. Due to the weight limitations to sent instruments to orbit, only detectors with small collection area can be used. Typically, they have large

Field of Views (as Fermi satellite). The HE observations are performed using a calorimeter, which technique is based on the pair production effect: when a γ ray reaches the detector, pairs of electrons and positrons are produced along a converter material. The amount of energy from the incident γ ray can be calculated through the number of pairs generated. Instead, for VHE an indirect technique needs to be used. This technique is called Cherenkov imaging technique. Its methodology consists of using the atmosphere as a calorimeter and large collection areas for the detectors.

Imaging Atmospheric Cherenkov Telescopes (IACTs) are designed to observe the Cherenkov radiation. This particular radiation is produced when a primary particle reaches the Earth's atmosphere ($\sim$ 20 km height), interacts with the existing particles in that layer and generates cascades or showers of particles that produce photons via this Cherenkov effect, which finally reach the ground telescopes (see Figure 9). Such particles travel faster than the speed of light in the medium, producing an emission that can be seen as short light pulses. This corresponds to optical (blue) emission which projection is recorded. The produced secondary particles and photons make the shower broader, so due to this effect the cascades are called Extensive Air Showers (EAS). For energies higher than $\sim$ 50 GeV up to $\sim$ 100 TeV, Cherenkov telescopes are much more sensitive than satellites.

From the information obtained from the Cherenkov radiation, it is possible to calculate the direction of this incident particle or γ-ray photon by the 'footprint' it leaves on the camera in terms of the size, shape and orientation.
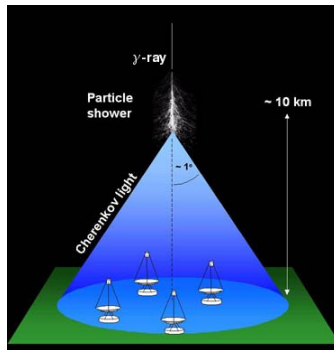

Fig 9. Schematic of Ground Based Gamma Ray Astronomy. Retrieved from: https://www.dur.ac.uk/cfai/vhegammaraygroup/physics/groundbased/

The mechanism behind is that the incoming highly relativistic charged particles polarize the molecules within the Earth's atmosphere. During the polarization, the atoms of these particles behave as dipoles, so they are oriented in a non-symmetric way just in the case the particle travelling close to them is relativistic. Finally, when the relativistic particle is far enough, the atoms are re-oriented to the initial position and emit Cherenkov radiation. All this radiation is transmitted throughout the atmosphere in a cone of angle θ_c whose center is around the primary particle incident direction. These Cherenkov photons are being absorbed by some scattering processes (such as Rayleigh and Mie) that attenuates the final radiation that reaches the light pool on the surface.

The particle cascades can be classified mainly in two types, according to the nature of the primary particle that reaches the top of the atmosphere (see Figure 10):

- Electromagnetic shower: They start with a γ ray as the primary particle and during the trajectory of the cascade, pairs of electron-positron (via pair production) and photons are created. The total number of particles increase while the cascade itself is being slowed due to the effect of the electric field by the particles present in the atmosphere. Geometrically, these kinds of air showers are compact and quite symmetric. In addition, cascades initiated by an electron show the same development structure. Therefore, it constitutes a source of background for γ-ray studies.

- Hadronic shower: These showers are generated by a CR that can be a proton or heavier nuclei, which interacts with a nucleon in the atmosphere and produces secondary particles which can be muons, pions, kaons and neutrinos, among others. If they are energetic enough, these secondary particles are able to produce other showers in the same cascade and also, the decay of π^0 can generate an electron cascade with this hadronic shower. The geometry of this kind of shower is broader, barely symmetric and more extensive than the electromagnetic one because protons and pions are usually more penetrating in the atmosphere and therefore, the hadronic cascades last longer than the electromagnetic ones.

  Since γ rays are a little fraction of CRs, all those CRs creating hadronic showers are the most important source of background noise for the detection of γ rays. Hadronic showers look irregular and some spreading in form of islands while muonic showers are tipically ring-shaped. Meanwhile, the electromagnetic ones have a typical elliptical shape when they are detected.
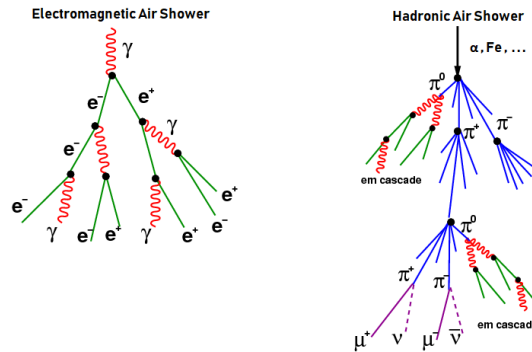

Fig 10. Left: Schematic example of an electromagnetic shower in which the primary particle is a γ ray. Right: Schematic example of an hadronic shower, where it can be seen the developement of the secondary particles and photons (Mollerach, S. et al., 2018).

The Cherenkov telescopes are focused at the maximum height where the cascades are formed, but not at the infinite as traditional optical/IR ground telescopes. The observation strategy on which these types of telescopes are based is illustrated in Figure 11: the mirrors are the ones in charge of focusing on the camera and, as the air showers are not concentrated in a single point, the images that we will see are scattered around the camera with different configurations depending on the type of the incoming cascade and positioned in terms of the angle between the telescope axis and the primary particle direction.
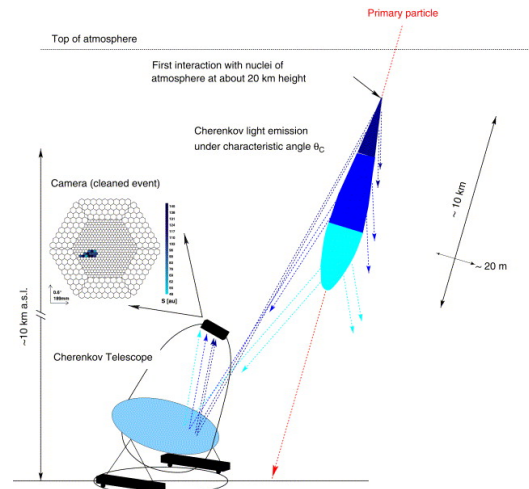
Fig 11. Scheme of the detection of γ-induced Showers with an Imaging Air Cerenkov Telescope. Retrieved from: http://ihp-lx.ethz.ch/Stamet/magic/magicIntro.html

In order to extract the useful information and where this γ ray have been exactly originated, the images are parametrized (see Figure 12). This parametrization is mainly based on geometrical parameters known as Hillas parameters, and it starts when the cleaning of the image from background noises is well done.

For a good characterization of the air shower, some of the Hillas and other image parameters are listed below, all of them used in the MAGIC analysis. It is important to note that each individual air shower is parametrized as an ellipse and then, the stereoscopic parametrization is calculated.

- Size: It is the total amount of Cherenkov light recovered by the camera for a single event.

- Length: This parameter corresponds to the measurement of the major axis of the ellipse. It gives an idea of the longitudinal development of the air shower.

- Width: This one represents the measurement of the minor axis of the ellipse. It shows the lateral development of the air shower.

- Dist: It gives the angular distance from the centroid of the ellipse to the expected source position in the camera. It requires a previous assumption about the possible localization of the source.

- Theta^2: This parameter gives the square of the angular distance between the reconstructed source position by the stereoscopic measurements and the real position of the source in camera coordinates. The showers coming from the source would be peaking at zero, while the background CRs would be randomly distributed.

- Number of islands: For the hadronic showers, the image projected tends to appear separated in various islands. This term gives the total amount of spacially separated 'islands' of pixels after the cleaning of the image.

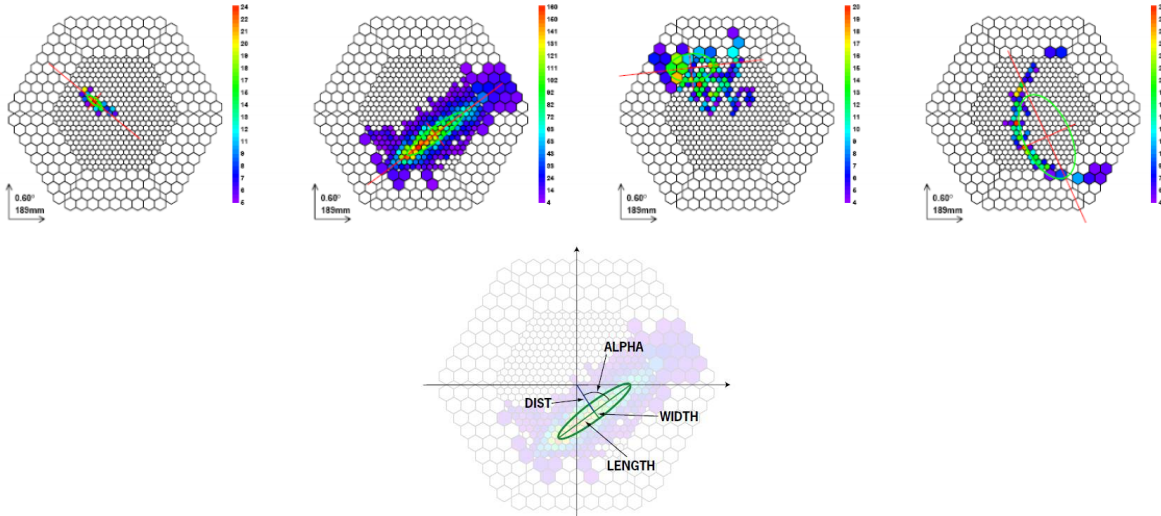Further information about the specific parameters can be found in the bibliography (see: https://magic.mpp.mpg.de/)

Fig 12. Above: Example of four different types of shower images recorded by the camera, all of them taken by the MAGIC telescopes. From left to right: electromagnetic shower, hadronic shower with quasi elliptical shape, hadronic shower with several islands and a muon ring. Credit: MAGIC collaboration. Below: Sketch of the projection of some Hillas parameters onto the camera of the MAGIC telescopes. Retrieved from: http://ihp-lx.ethz.ch/Stamet/magic/parameters.html#ShapeParameters

1.5 Telescopes description/outlook

In order to put in context the data of HE and VHE with which we are going to work later, it is convenient to know the basic characteristics of the telescopes as well as the operation of their instruments and how they usually work to take the data. Both MAGIC and Fermi-LAT are the telescopes from which we have analyzed the information of our source and thus, they are going to be briefly explained in this section.

1.5.1 The MAGIC Telescopes

The MAGIC (Major Atmospheric Gamma Imaging Cherenkov) telescopes, also called The MAGIC Florian Goebel telescopes, constitute a system of two IACTs, MAGIC I and MAGIC II, located at the Observatorio del Roque de los Muchachos on the Canary Island of La Palma at 2230 m of height.

Both have a diameter of 17 m, with a collection area of 236 m^2 and they were built with light materials so the total weight of each telescope (72 tons) is not a problem for a fast rotation. In addition, they do not have a dome, so the three-layer structure must be resistant to endure the bad weather days. The pointing system of the telescopes works really fast, so they can rotate to any orientation in the sky in less than ∼30 seconds. It was designed to be able to move fast for GRB alerts, due to this kind of phenomena are extremely fast.

The characteristics of MAGIC II (which was constructed a few years later than MAGIC I) are practically the same of MAGIC I except for some improvements on the overall sensitivity and stability. They work on stereoscopic mode to improve the characterization of the air showers. However, each telescope measures its own data and then, during the data reconstruction, these independent files are transformed into stereoscopic measurements.

With respect to the energy ranges, MAGIC I and II can observe VHE γ rays above ∼50 GeV.

Fig 13. The MAGIC telescopes at the Roque de los Muchachos Observatory. Credit: Lucía González Cuesta.

Due to the movement of the reflecting surface, the mirrors can suffer from misalignments mostly caused by the deformation in terms of the zenith angle. To solve this problem, the Active Mirror Control (AMC) technique uses a total of 250 lasers (controlled via online using 'look up tables' or LUTs) and they let us know if the panels which are part of the great structure of 240 m^2 are correctly focusing on the camera (see Figure 14).
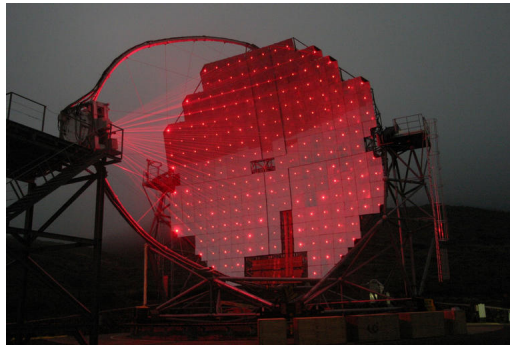
Fig 14. Picture of the Active Mirror Control in operation for one of the MAGIC telescopes. Retrieved from: https://magicold.mpp.mpg.de/gallery/pictures/

The electronics of these telescopes are formed by the following elements that should be highlighted:

- The camera: it is formed by Photomultiplier Tubes (PMTs) that improve the quantum efficiency of the detector and it covers a FoV in the sky of 3.5 degrees.

- The starguider: it consists of an additional CCD camera, which is in charge of calculating any possible mispointing in the tracking system by comparing the star positions of the FoV with an existing catalogue of the same zone.

- The trigger: due to the high background not all the information is saved. This system rejects those showers that do not look like as γ-types. Each telescope has its own trigger, but when they work together (standard case) there is a stereo trigger connected between them that results much more efficient.

- The readout system: the showers which full fill the trigger criteria are digitalized. As the γ-ray signals are really short, a quite fast system to store the data is needed.

- The calibration system: we take data with standard trigger at ∼300 Hz, so this system manages the conversion of the data acquired by the readout system to light flux that falls on the camera. In order to do that, light pulses are injected to calibrate the flux.

- **Observation modes**

The IACTs observe typically in two modes: ON-OFF mode and Wobble mode. Within the ON-OFF mode, the observations are performed pointing to the target, i.e. the target falls in the center of the camera (where the sensitivity is the maximum). To measure the background, in addition to the observation of the source (ON data), a source free region is needed to be observed as well (OFF data).

In contrast to the ON-OFF mode, the Wobble mode consists of changing the observing position of the source by 0.4 degrees from the center of the camera. In this observation mode, the ON and OFF data are taken simultaneously. Every 20 minutes, the pointing of the source changes 180° off-axis since it measures the Wobbles in pairs, getting 4 different final positions for the same source while we are also taken OFF data from the other 3 left positions. If we look at Figure 15, the procedure to follow in this mode could be, for example, a configuration where the source is pointed at W1 and W2, W3, W4 are the backgroumd positions. In these three positions W2, W3 and W4, we are obtaining information of background events to achieve an estimation of the night sky background (NSB) close to our source, while in W1 we are capturing the photons coming from the desired source. After 20 minutes, the source position changes, and now it is pointed at W2 while W1,W2,W4 are the positions where the background is captured by the camera. And so, the pointing of the source will be changing every 20 minutes between Wobble pairs (W1-W2 and W3-W4). In Figure 15 are illustrated these Wobble positions.

It is important to know the advantages and disadvantages of each mode to be able to decide which one is the best depending on the case. On the one hand, the ON-OFF mode is more sensitive because it always point to the center of the camera, however, it requires additional observation time to take both measurements. So maybe the weather conditions could have changed between the ON and the OFF data times and therefore, they could not be correctly treated later.

On the other hand, the Wooble mode is a bit less sensitive because it works out of the center of the camera added to that the assumption of the camera homogeneity is not completely real. Nevertheless, when we are using this method, we are saving observation time and also having the OFF data under similar conditions as the source data, since all the data is collected at one time.
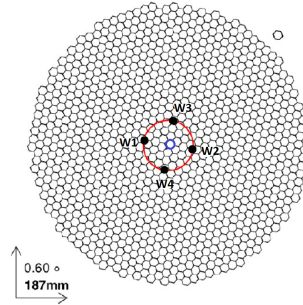

Fig 15. Schematic picture of the Wobble mode in the camera, where it is shown the four Wobble positions chosen (Alicia López-Oramas, 2015).

1.5.2   The Fermi Large Area Telescope (LAT)

The Fermi Gamma-ray Space Telescope is a space-based observatory launched in 2008 to observe and study HE γ rays. It carries two instruments on board called Large Area Telescope (LAT) and Gamma-ray Burst Monitor (GBM), for different purposes. The experiment covers a large energy range from $\sim$8 keV to $\sim$300 GeV. The LAT instrument, which is the main instrument, is covering the range of γ rays from $\sim$20 MeV to $\sim$300 GeV. These such low energies cannot be observed from ground and the VHE of the order of hundreds of GeV are also impossible to detect from space. Therefore, the combination of the IACTs and space telescopes as Fermi-LAT is crucial to be able to study the entire range of γ-ray energies.

As commented before, space-based telescopes cannot use large effective areas due to restrictions on the payload mass, so the effective area of the LAT instrument is very limited, being 8000 cm^2 at E > 1 GeV. This instrument operates in a survey mode scanning the majority of the observable universe in HEs. Besides, it owns a wide Field of View of about a 20% of the entire sky and its sensitivity is very high for E > 10 GeV. Thanks to that, it can cover the entire sky every 3 hours changing the orbit north-south alternatively. In addition, this observatory is able to point a target of opportunity when it is needed, as a secondary observing mode.

Fig 16. Illustration of the Fermi-LAT as it would be seen in orbit. Retrieved from: http://www.ung.si/en/research/cac/projects/fermi-lat/

The detection principle that measures the γ rays is based on two main facts: first, the usage of an anticoincidence system to do a correct background rejection of the CRs that come to the surface of the instrument, and second, the application of the pair production principle, which is basically the decomposition of a γ ray in a pair of electron-positron by a converter material. The size of the Fermi-LAT is 0.72x1.8 m and it has a total mass of 2789 kg. It is composed by four subsystems, all of them working together to detect γ rays and to reject the signals coming from the CRs (see Figure 17). These components are: Tracker, Calorimeter, Anticoincidence detector (ACD) and Data Acquisition System (DAQ).

The ACD is the first component in charge of rejecting the cosmic rays generating light flashes every time a CR hits its surface. The Tracker measures the 'footprint' that the pair of electron-positron has left throughout the trajectory since the initial γ ray was decomposed. Then, the Calorimeter measures the incoming energy of this pair of particles and it is also useful to reject CRs because the pattern of the energies results different between each other. Finally, the DAQ makes the definitive distinction between a real γ ray and a CR (or a γ ray produced in the Earth's atmosphere) by reading all the information coming from the other elements of the LAT to decide which data are saved.
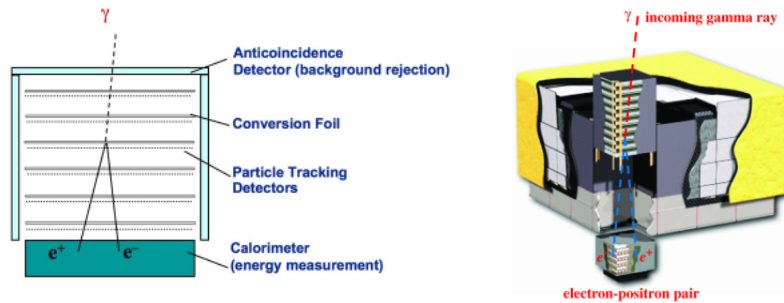

Fig 17. A 2D Scheme of the principles of operation (left) and a 3D construction model (right), both of the LAT instrument. Retrieved from: https://www-glast.stanford.edu/instrument.html

2   Motivation and Goals

2.1   Overview of blazar OT 081

The source OT 081 (also known as PKS 1749+096 and 3FGL J1751.5+0939) studied in this work is a blazar, classified as a BL Lacertae object, and subclassified as an LBL[1] according to the blazar sequence. BL Lac objects (BLL) are those characterized by the absence of emission lines in their spectra or if appear, they are extremely weak. Its redshift (z = 0.322) was measured from spectroscopic observations (Stickel et al., 1988). The given coordinates in Right Ascension (RA) and Declination (DEC); (J2000.0) based in radio observations (Johnston et al., 1995) are: $RA = 17^h51^m32.815^s$; $DEC = +09°39'0.728''$[2].

According to the latest publications, the blazar OT 081 has already been studied in optical (imaging and spectroscopy for the morphology and redshift estimation, classification and time behavior) and

---

[1]Classification extracted from TeVCat (www.tevcat.uchicago.edu)

[2]Coordinates extracted from NED database (https://ned.ipac.caltech.edu/)

infrared, as well as VLBI multi-wavelength observations and polarization in the $\lambda = 6$ cm. The source was included in the gravitationally lensed blazar candidates which study was carried out using radio maps from the 1 Jy BL Lac sample. No macrolensing was found for OT 081 but they do not rule out the microlensing effect (Rector et al., 2003). In addition, observations about the possible correlation between optical and radio have been done by studying the flux variations in both frequency ranges of a sample of extragalactic AGNs. They did not found any strong hint correlation between optical and radio, but they discovered a correlacion between two radio frequencies, 37 and 22 GHz (Tornikoski et al., 1994).

Finally, Fermi-LAT and MAGIC gave notice of a flare from OT 081 in 2016. Fermi-LAT alerted (ATel #9231) an MAGIC followed up (ATel #9267), in order to have a first detection of VHE radiation of this source. Besides, there is another notice (ATel #9260) in which it was found optical correlation in the outburst activity with respect to Fermi-LAT and Swift data, so they encouraged new multi-wavelength observations for a deeper study of this particular source.

2.2   Objectives

The main goal is to analyze this source in the VHE band for the first time. Since only a very limited number of sources of this type are known ($\sim$76 VHE sources and only 2 LBLs), it is very important to characterize each of the sources individually. We should also take into account that it is really essential to perform the study of this source in a multi-wavelength (MW) context in order to follow up closely its activity. In the same way, possible correlations at different energies could be found in the observations. Besides, this multi-wavelength characterization allows us to know better the emission processes inside the jet. For this particular source, the telescopes detected a flare in the optical, followed by a notably increasing in its flux in the γ rays and X rays ranges that came from the same source and simultaneously. This leds us to keep studying this source because there is an unprecedented activity of γ rays when these flares occur.

Throughout this work, our aims are analyzing the VHE data from MAGIC and HE data from Fermi-LAT for OT 081, in order to obtain the SED, the Light Curve and Skymaps. This information at γ rays will be studied in a MW context including data from radio, optical and X-rays along with the Fermi-LAT and MAGIC data. An emission model will be proposed using the theoretical scenario of Synchrotron Self-Compton (SSC) of the jet emission for a detailed and deeper study.

3   Data reconstruction

3.1   Analysis of MAGIC data

The MAGIC analysis chain is designed to reconstruct the path of the γ ray since it departs from its source, travels through different space environments and reaches the Earth's atmosphere until it is finally captured by the camera. It is important to take into account all the possible processes involved

as well as the background sources. In order to do that, a software called MARS (MAGIC Analysis and Reconstruction Software) based on the analysis software ROOT which uses the C++ programming language was developed. MAGIC I and II work in stereoscopic mode, although each telescope store the data indenpendently. There are mainly three data types that are necessary for the MARS analysis chain:

• **On/Off data from telescopes:** On data correspond to the observations of the interested source. In our case, we chose the Wobble mode, so the background measurements will come from the same observations. Off data are basically observations from other FoV in which there are not γ rays expected. These last observations are going to be used during the analysis chain, to distinguish between γ-ray events and hadronic showers.

• **Monte-Carlo (MC) simulations:** this kind of data is used to differentiate whether the air shower is electromagnetic or hadronic, when the gamma-hadron separation step is done. It is a way to train the system to be able to simulate the behaviour of a real γ ray and thus, to have a good comparison of the main parameters between the real and the simulated images.

• **Auxiliary data:** these files or runs give general information regarding weather conditions, technical information and other additional facts about the telescopes.

Crab observations: these correspond to On observations (also in Wobble mode) from the Crab Nebula. Due to the fact that the calorimeter is the Earth's atmosphere, no calibration of the instrument is possible in that case. Because of that, it is used the Crab Nebula for the calibration. This particular source is considered as a standard candle because its emission is strong and it has not been observed any variability yet in VHE. Therefore, the calibration is made using these observations to ensure that the analysis chain is being correctly done.

Three different types of reconstruction levels are used during the analysis chain: Low, Intermediate and High Levels.

- *The Low-Level Data Reconstruction* does the image cleaning and the image and timing parametrization.

- *The Intermediate-Level Data Reconstruction* starts with the data quality selection followed by the stereo calculation. After that, it performs the calculation of Hillas parameters and ends with the event classification (gamma or hadron) and the energy estimation.

- *The High-Level Data Reconstruction* is in charge of estimating the γ-ray signal from the source and finalizes with the spectrum calculation as well as the skymaps and light curves.

For this work, we started with the data files given by the MARS executable called Star. This is

the one that results from the calibration during the Low-Level and give us the files with Hillas parameters. All the previous reconstruction was already done for this source because the cleaning represents the most tedious and difficult part in the analysis chain. The following subsections will provide a description about all the analysis steps we have followed during the analysis chain of the source.

3.1.1 Data quality selection

In this first part of the analysis, the goal is to verify the weather and moon conditions of our data, individually for each observation date. If an overall good quality is considered, then we call them as dark data. Since the Star files are divided into MAGIC I (M1) and MAGIC II (M2) data, it will be enough to do the check to M1 data because both telescopes observe simultaneously.
All the On/Off observations are checked for: The Mean Discriminator Threshold (DT) vs Time, The Rate vs Time and The Pyrometer.
The first one represents the DT with respect the time. This DT value corresponds to a fixed limit which tells us about the night sky conditions. The lower the DT the larger is the saved amount of data with lower energy threshold. In case of moonlight nights, the DT should be higher to avoid saving too much background events. We consider a good quality when this DT is the lower as possible, because the lower the energy threshold the better. A DT value $\lesssim$50-60 and stable is acceptable for a good quality.
Secondly, the Rate vs Time graph gives the number of saved events with respect the time. This number should be high (typically between $\sim$200 and $\sim$300) and the tendency quite constant over time.
If a considerable variability is seen, then the data have been affected by bad weather conditions and/or other bad quality effects.
Within the Pyrometer, the temperature, the wind speed and other parameters are measured. Taking into account all these weather conditions it can be constructed the Cloudiness parameter. This is basically the probability of having or not clouds, and that means, a worse or better quality of the data. A good value for the Cloudiness is accepted when it is around or below 30-40% and the tendency is practically flat over time.

With respect to the dates, the data from Off sources are from September, 2016 and the On data are from July, 2016. Only one day (22-07-2016) had to be removed from the whole observation in the case of the On data, due to bad conditions caused by moonlight. The rest of the days, 25,26 and 28 of July were successfully selected and taken under dark conditions.

In Figure 18, some examples of the three previous plots in the case of both good and bad quality conditions are given:
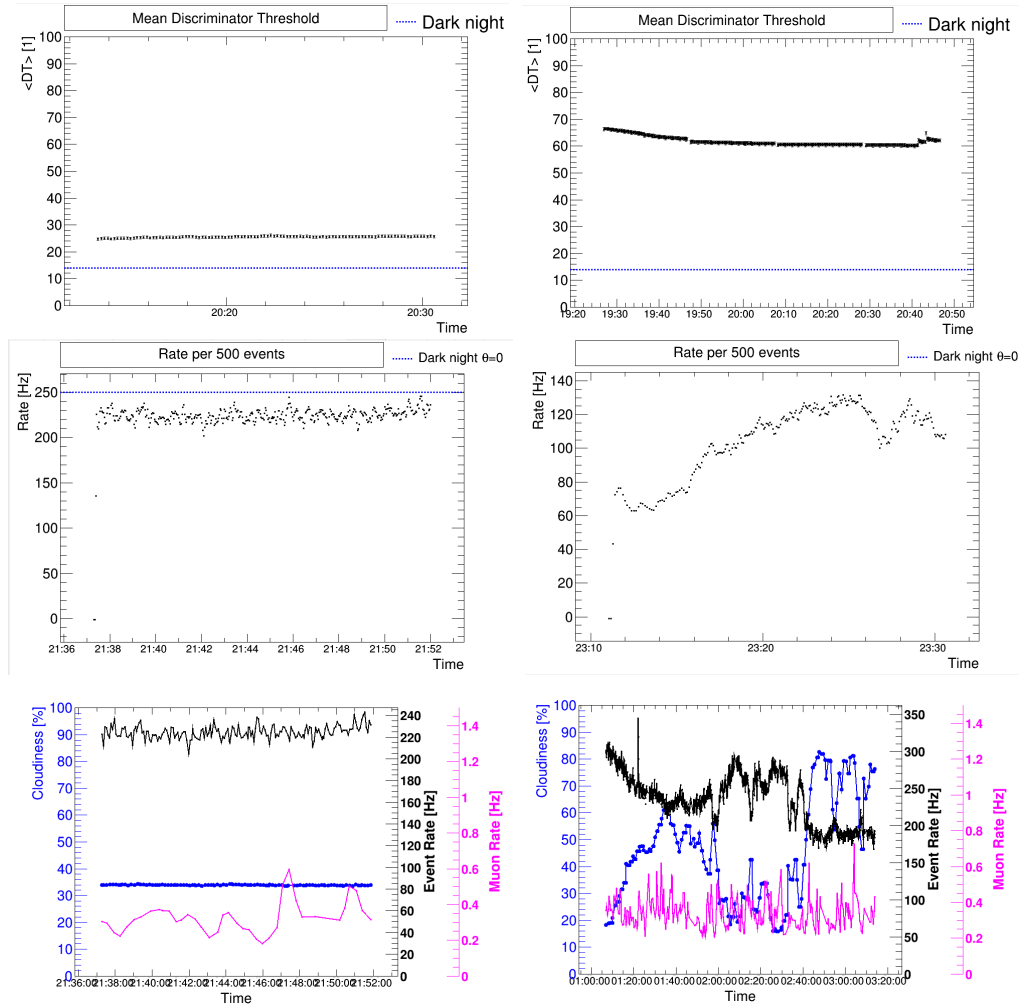
Fig 18. Comparison between good (left column) and bad (right column) quality plots, in terms of three parameters: Mean Discriminator Threshold evolution (upper panel), Rate evolution (middle panel) and Cloudiness evolution (lower panel).

3.1.2   Calibration

SuperStar

This executable is made for joining the independent M1 and M2 Star data in stereoscopic files. The aim is to reconstruct the shower parameters for the stereo mode, by identifying those pairs of images (M1 and M2) that belong to the same event. This routine is applied to On/Off data and also to the MC files.

Coach

In this executable, our data is not processed but only a Random Forest algorithm is used to learn how to classify γ rays and hadronic showers with respect to their parametrization and timing information.

It is based on the construction of decision trees (using several variables which are generally correlated) in order to estimate the energy and the gamma-hadron separation. This last estimation can be done by the hadroness parameter, which covers values from 0 to 1. Basically, it gives the probability that the event was caused by an hadron (values closer to 1) or by a γ ray (values closer to 0). In the case of the energy, which is obtained from the image parameters, two possible tools are given: estimation via Random Forest or via the creation of Look up Tables (LUTs). For this work, we have chosen to do the reconstruction by LUTs.

Within this step, the data needed are the Superstar Off observations and a type of Superstar MC data called 'train'. On the one hand, the Off observations give the information about hadronic showers. The MC simulations are separated in two different data samples according to each purpose for the analysis chain. These specific MC 'train' data are created for the training with Coach, which simulate γ rays penetrating the telescope; and there are other MC 'test' simulations that will be used later in the analysis chain to obtain the spectrum of the source. So, Coach is in charge of comparing the Off observations and the MC train simulations to be able to obtain the hadroness parameter and the energy of each event.

Before running Coach, its configuration file (coach.rc) must be modified first. The parameters that we edited were the path to the MC train files and Off files, the output location and the minimum and maximum zenith angle of the set data. The reason of choosing a range of zenith angles is because the air shower changes its shape depending on this parameter. So, it is important to use the same zenith angle range than the data of the target we are analyzing when running this routine. We have selected the Off data and MC train data that covered a range that ensure the On observations (which will have a smaller coverage of zenith angles, from ZA = 19 to ZA = 26) are included in that range of zenith angles.
The results for Off and MC train data sets are from ZA = 12 to ZA = 63 and from ZA = 4 to ZA = 63, respectively. We performed the training using the Off zenith angle range because the MC train range did not cover the Off data from ZA = 4 to ZA = 12.

Melibea

This executable is in charge of the energy reconstruction process and the event classification. It applies the learning obtained in Coach about the classification of events, to the data from the source (Superstar On files) and MC files from the 'test' data. It is possible thanks to the information provided by the outputs of Coach which designates an energy and a hadroness parameter (it quantifies the probability of an air shower of being a hadron or a γ ray) to each event.
At this point, the intermediate analysis ends to make way for the Standard High-Level reconstruction.

3.1.3   Detection

Odie

In order to check the emission of the source of interest, Odie makes $theta^2 (\theta^2)$ plots (plotted as ON and OFF histograms), where the significance values for the source are given. The parameter θ means the difference between the nominal source position in the sky and the air shower reconstructed position. Therefore, we expect to have a plot with a peak in lower values of θ^2, followed by a decrease at higher θ^2 with a lower and constant background. The significance is calculated by the Li-Ma formula, defined by Equation (2).

$$S = \sqrt{2} \cdot \left[N_{ON} \cdot ln \left(\frac{1 + \nu}{\nu} \cdot \frac{N_{ON}}{N_{ON} + N_{OFF}} \right) + N_{ON} \cdot ln \left((1 + \nu) \cdot \frac{N_{OFF}}{N_{ON} + N_{OFF}} \right) \right]^{1/2} \qquad (2)$$

Where N_{ON} and N_{OFF} are the number of events in the signal region from ON and OFF regions, respectively and ν is the normalization factor between the ON and OFF distribution.

According to that, some parameters of the odie.rc configuration file must be edited first. The analysis can be performed at different energy cuts: Low Energy (LE), Full Range (FR) and High Energy (HE). The cuts are optimised for the Crab Nebula but they can be also used for other sources. In our case, we chose LE and FR because the source of this study does not reach the higher energies within the VHE range. In addition, the analysis epoch has to be chosen (Jan10, Jun10 or Jul13) because the performance of the instrument may change. In our case and for this source, we put the most recently one: Jul13. Finally, as we are working in Wobble mode, we chose three OFF regions (N_{OFF}) to calculate the background for the signal search.

We will consider a positive detection of our source if the significance is over $\sim 5\sigma$. For the case of FR, this value is not successfully achieved in neither of the dates or the total set of dates (an example is given in Figure 19). However, for the LE case we are sure that we have a detection of this source when analysing the total set of dates and the first day independently (significance $> 5\sigma$). For the days 26 and 28 the significance was under 5σ. Therefore, the emission mainly come from the first day. The other two days are considered upper limits in the detection because they do not reach the required value independently (no 'significant' excess of events). In Table 1 it is detailed the results obtained for each of the days. In addition, the LE range output plots for the first day of data and the total set of dates are shown in Figure 20.
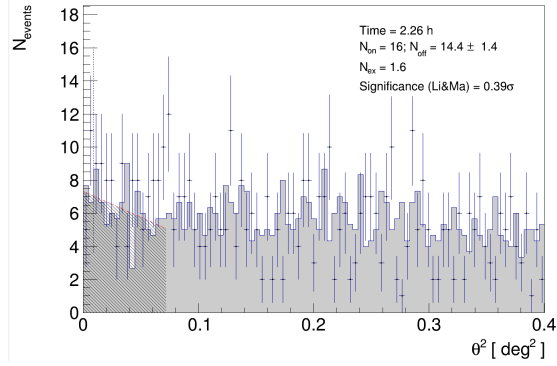
Fig 19. Distribution of the squared angular distance θ^2 considering a full energy range (FR), for events in the direction of OT 081 (blue points) and normalized off-source events (grey histogram) for data taken on the 25th, 26th and 28th of July 2016.
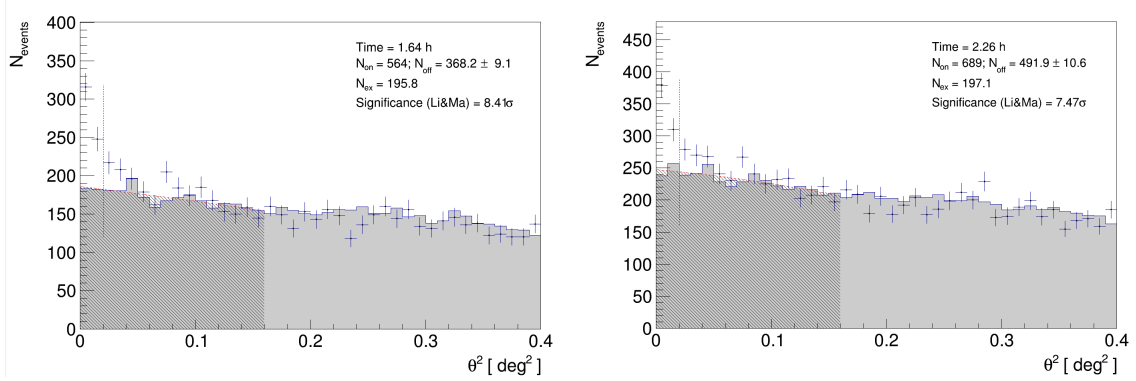

Fig 20. Distribution of the squared angular distance θ^2 considering a low energy range (LE), for events in the direction of OT 081 (blue points) and normalized off-source events (grey histogram) for data taken on the 25th of July 2016 (left) and 25th, 26th and 28th of July 2016 (right).

DATES	Significance (FR)	Significance (LE)	Time of observation (h)
25-07-2016	0.54σ	8.41σ	1.64
26-07-2016	0.00σ	0.78σ	0.31
28-07-2016	0.00σ	-0.41σ	0.30
All dates	0.39σ	7.47σ	2.26

Table 1. Significance and observation time values for the events from the source OT 081, calculated for two different energy cuts (FR and LE) and for each of the dates and all the set.

Caspar

This executable creates intuitive skymaps created from Melibea outputs. To be able to obtain a skymap, the reconstructed arrival directions of all shower images are transformed into sky coordinates. While performing a skymap, one can estimate the ON/OFF ratio in the whole FoV of the telescopes. Within the configuration file (caspar.rc), it can be chosen different energy cuts (LE, FR and HE as Odie) and the analysis epoch. We selected the same options as in the case of Odie, but for this task,

only the total set of dates is used.

The main output plots we are most interested in are the Test Statistic (TS) value map and distribution, which are useful to verify if the source is detected. We can see these results for both energy ranges (FR and LE) corresponding to our source in Figure 21.

If we look at the TS value map and TS value distribution for the LE case, it is clear that our source appears as a well-defined point like source. Besides, there is a deviation in the distribution of the TS value beyond the Gaussian red line distribution, which represents the expectation of random event distribution. It gives us the notice that we have a detection for this energy range. Meanwhile, for the FR case it is confirmed once again we do not have emission in that domain. So, it is confirmed that our source is a low energy emitter, as we already saw in the θ^2 plots.
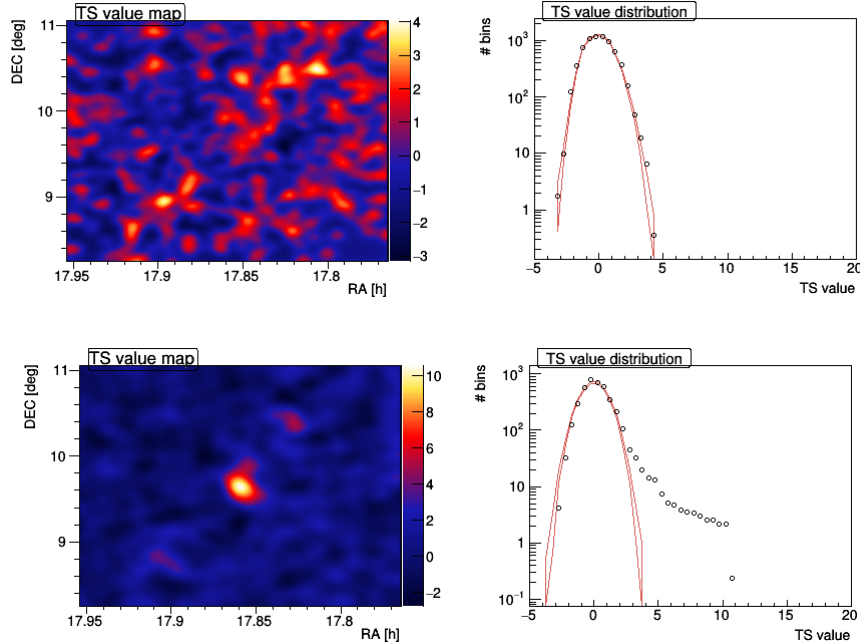

Fig 21. Above: Full Range Skymap (left) and distribution of the TS value (right) from OT 081, during a flare state on the 25th of July 2016. No detection of the source for this energy range is achieved. Below: Low Energy Skymap (left) and distribution of the TS value (right) from OT 081, during a flare state on the 25th of July 2016. Sucessful detection for this energy range is obtained.

Flute

In this executable, the Spectral Energy Distribution (SED) and the Light Curve (LC) are calculated. In order to estimate the flux values, the Melibea outputs of the On data and the MC test simulations are used. As we mentioned before, these last are required to correct from instrumental effects and used to calculate the collection areas for the spectra. Another important parameter for the flux determination is the number of γ rays, which is obtained from the θ^2 distribution for each energy bin. Therefore, a binning of the data using an estimated energy will be also done. In principle we can use the default parameters of number of bins and the minimum and maximum Estimated Energy.

As in the previous executables, first we need to edit the configuration file (flute.rc) and then we will run it for each of the On dates separately.

In first place, the minimum and maximum zenith angle of this set of data will be needed. These will be necessary for the calculation of the effective collection areas, which also depend on the γ-ray incident energy and the applied cuts of energies. The following values of the zenith angle for each date and the entire set are given in Table 2.

DATES	ZA(min)	ZA(max)
25-07-2016	19	26
26-07-2016	22	25
28-07-2016	20	22
All Dates	19	26

Table 2. Minimum and Maximum zenit angles of On data from each of the dates and all the set.

As we want to build the LC correctly, we must choose some energy parameters. Two of them ask for the minimum and maximum energy limits (both in GeV) used to calculate the flux. In our case, we left the default values just to check the energy range covered by our source data and then we changed the values to: flute.EminLC: 100, flute.EmaxLC:inf (that means the flux will be obtained above the Emin value). The third parameter is asking for the selection of the energy binning with respect time. Here there are two options to choose: night-wise (most common one) or run-wise. The run-wise option corresponds to the time binning of the LC and it is useful for checking if we have systematic effects (that may have come from different positions in the camera). We used both of them and they gave compatible results as we did not detect intra-night variability, so we decided to choose night-wise option to work with the plots henceforth.

According to the SED plot, only two input fields were modified: the redshift of our source (z=0.322) and the assumed spectrum fit. This last parameter corresponds to the theoretical fit type used for our data. The default value is given by the intrinsic spectrum of Crab Nebula. If we run the executable once just for testing the kind of fit applied to our data, we will have a trial SED and thus verify the energy range covered by the source.

The VHE observed spectrum can be well-described by a power law with a photon index (Γ) and a normalization constant, F_0 at energy E_0 of the form given by Equation (3).

$$F = F_0 * (E/E_0)^{-\Gamma} \tag{3}$$

Here, E_0 is ~150 GeV for our data and Γ is calculated from our source spectrum data, following an iterative process until it reaches a stable value. If the slope does not change too much between two consecutive trials of Γ, then we consider that the fit is good enough. For those days without detection (upper limits: days 26 and 28), it is assumed the same Γ as for the detection (first day of observation). In Table 3 we can see these values, along with the results for the integral flux and its error in the case of the LC. As the two last days are upper limits and not measurements, their integral fluxes do not

have associated errors.

DATES	Γ	$f\,(cm^{-2}s^{-1})$	$\triangle f\,(cm^{-2}s^{-1})$
25-07-2016	4.36	$6.0434\cdot 10^{-11}$	$\pm 1.05279\cdot 10^{-11}$
26-07-2016	(U.L.) 4.36	(U.L.) $2.60851\cdot 10^{-11}$	-
28-07-2016	(U.L.) 4.36	(U.L.) $1.08228\cdot 10^{-10}$	-

Table 3. Measured spectral photon index , integral flux and its error of On data from each of the dates and all the set.

The results achieved within this executable for the total LC (E > 100 GeV) and the SED of the first day (25-07-2016), are shown in Figures 22 and 23, respectively.
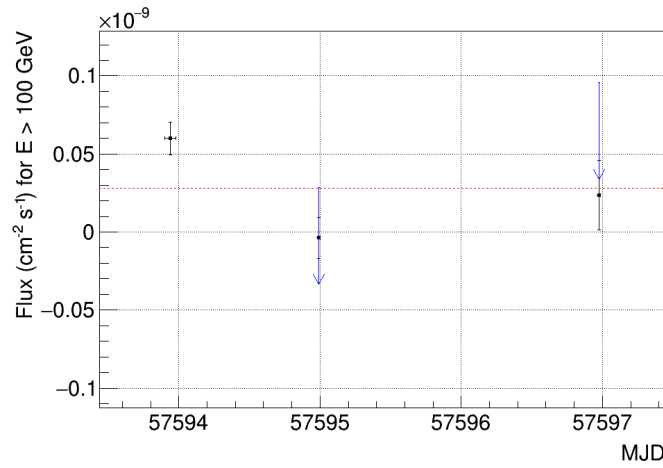

Fig 22. Light curve of OT 081 above 100 GeV, for the whole observation of MAGIC during a flare state on July, 2016. The black points represent the flux calculated for all the days. However, because the last two points are not significant an upper limit is calculated. The blue arrows indicate these upper limits (UL) from the two last days of observation (26th and 28th of July 2016), with a non-detection of the source.
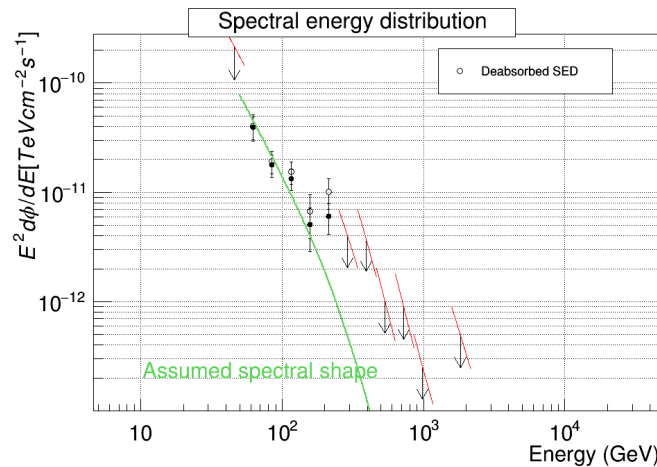

Fig 23. Spectral Energy Distribution (SED) of OT 081 as measured by MAGIC, during a flare state on 25th July, 2016. The black dots represents the spectrum and some upper limits are shown as black arrows. The open circles show the de-absorbed spectrum after the EBL-correction applied by the task of Flute. The best fit to the data is represented by the solid green line, which corresponds to a power law function applied.

- **Unfolding**

This step corrects for instrumental effects, which typically depend on the assumed initial spectrum. It does a transformation from an observable, in our case the Estimated Energy (Eest) to a physical quantity, the True Energy (Etrue), and the outcome is saved in the migration matrix. This step is crucial to obtain a better data fit in the energy distribution, due to the Eest is being influenced by a limited resolution and a possible bias.

In order to do that, a root macro called CombUnfold.C and its configuration file (combunfold.rc) were used. The macro file must not be modified in any case, but only the parameters of the configuration file will be edited during the process. CombUnfold.C estimates the true energy of an event from its reconstructed energy, using the information from the Flute outputs as input files.
As we already saw, only the first day of the set of dates gives a positive source detection, so the Unfolding step will be only applied to this day (25-07-2016).

Inside the configuration file, dfferent Unfolding models can be chosen: Forward, Tikonov, Schmelling, Schmelling Minuit, Bertero and Bertero W. The Forward Unfolding does not work with series of spectral points but it works with statistical calculations. Its spectral shape is assumed analytical so in the resulting plot it is given the parameters of a function (so that, it is just a fit). The Forward model is useful to test the method and then to apply the best input parameters to the others Unfolding models.

The main commands inside the combunfold.rc are associated to the number of spectrum iterations, the bin ranges of Eest and Etrue to be used in the unfolding (both manual or auto select options are available), the unfolding type model, the fit function type to the model and the optional parameters of that function.
For our case, we chose a total of three iterations and we started with a Forward model, using the bin auto selection for Eest and Etrue. A power law fit function was selected because it achieved the best fit to our data, and we also fixed the normalization constant to 0.1 TeV. Once the configuration file was saved and executed, we pay attention to the output graphs and we select the best bin range for Eest and Etrue manually.

In Figure 24, it is shown the event selection for the Forward Unfolding, along with the migration matrix, the collection area and other parameters.
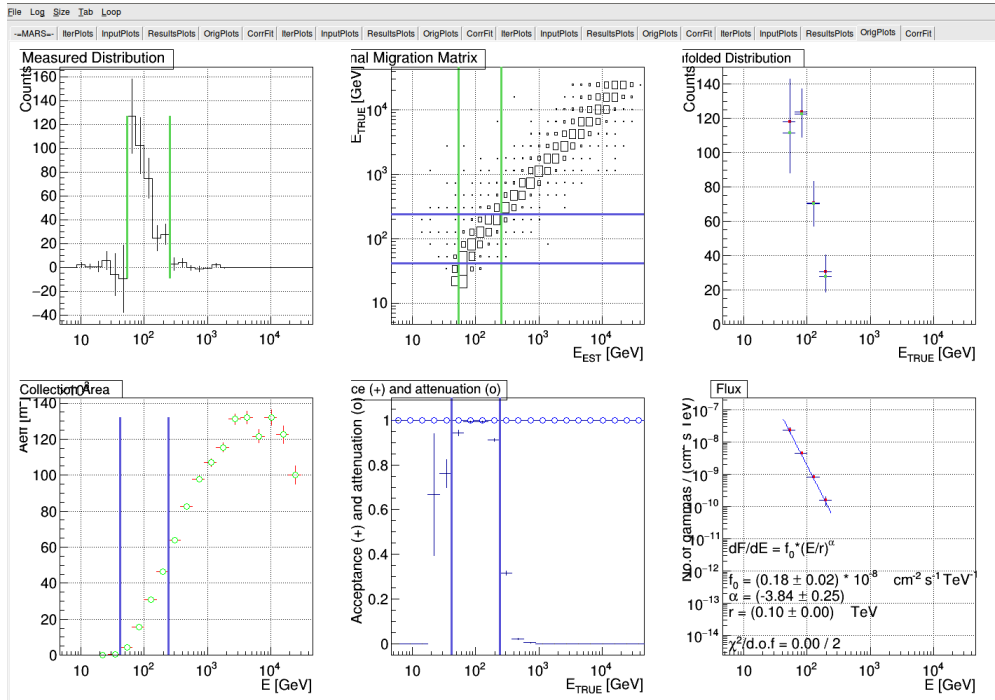
Fig 24. Original plots of the Forward Unfolding method for the third iteration, as seen in the output of the Unfolding step.

Next step is to execute the Forward model again but with the minimum and maximum bin parameters for the energies as the new inputs. Finally, we change the Unfolding model one by one until their plots have been saved correctly. The representation of all the models together (distinguished by different color plots) over the Forward Unfolding is shown in Figure 25. All the results obtained were compatible with the desired fit, so we choose the Tikonov model data for the SED plot.
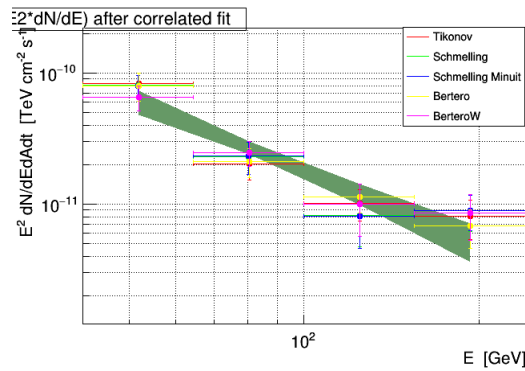

Fig 25. SED of OT 081, as measured by MAGIC, on the 25th of July 2016. The green shaded area represents the statistical uncertainties of the analysis given by the Forward Unfolding method. All the different Unfolding methods used are represented in coloured dots for an illustrative comparison.

- **EBL modelling**

After applying the Unfolding to the outputs of Flute, the macro CombUnfold.C gives also the possibility to carry out the EBL-correction.

Therefore, an Unfolding model is chosen (in our case, the one called Tikonov) while various EBL data models are tested one by one. Three different state-of-the-art EBL models were tested: EBL Dominguez (2011), EBL Franceschini (2008) and EBL Kneiske (2010).

At the end, the results of each one were compatible so we decided to choose the EBL model by Dominguez et al. to represent the MAGIC SED, because it is one of the current models used in other similar studies. In Figure 26, it can be seen all the models together in comparison with the Tikonov Unfolding model before the EBL correction. Besides, in Table 4 are detailed the different parameters of the fit for the SED, obtained for each case.
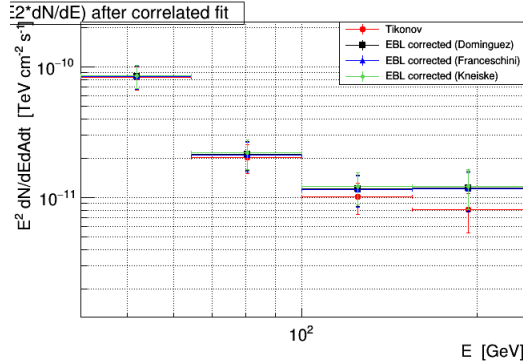

Fig 26. SED of OT 081, as measured by MAGIC, on the 25th of July 2016. The Tikonov unfolding method results are shown as red circles. Different EBL correction models are applied to the Tikonov data. EBL model by Domnguez et al. (2011), EBL model by Franceschini et al. (2008) and EBL model by Kneiske (2010) are shown by the black squares, the blue triangles and the green diamonds, respectively.

Model	$f_0 \, (cm^{-2}s^{-1}TeV^{-1})$	Γ	χ^2
Tikonov	$(1.87\pm0.20)\cdot10^{-9}$	3.86 ± 0.43	2.82
Tikonov EBL Dominguez et al.	$(2.14\pm0.24)\cdot10^{-9}$	3.66 ± 0.45	3.67
Tikonov EBL Franceschini et al.	$(2.10\pm0.24)\cdot10^{-9}$	3.67 ± 0.45	3.71
Tikonov EBL Kneiske et al.	$(2.19\pm0.25)\cdot10^{-9}$	3.63 ± 0.45	3.59

Table 4. Values of the power-law fit to the SED with $E_0 = 0.1$ TeV, for observed spectra unfolded using Tikonov and for observed spectra unfolded Tikonov EBL-corrected by three different models: Dominguez et al., Franceschini et al. and Kneiske et al.

Crab analysis

The IACTs use the Crab Nebula as a standard candle, in order to obtain a good calibration to test the analysis chain, as we have mentioned before. In this work we also did this calibration to ensure the veracity of the results.

Crab data from the day 29th September, 2016 were analysed choosing the LE energy cut and 3 Wobbles, with a total observation time of 1.62 hours and reaching a significance of 47.33σ (see Figure 27). After the quality selection of the data and all the calibration and detection steps, the SED was calculated. The fit to the Crab data is given by a log parabola assumed spectrum given by the Equation (4).

$$F = F_0 * (E/E_0)^{-\Gamma_1 - \Gamma_2 * log(E/E_0)} \tag{4}$$

Where F_0 is the normalization constant at E_0, Γ_1 is the spectral index and Γ_2 is the curvature parameter, both of the log parabola function. As a result, the final plot is represented in Figure 28. By looking at this plot, we can verify that the calculated Crab SED (green line) is compatible with the previous results from the bibliography. Therefore, our analysis chain is validated.
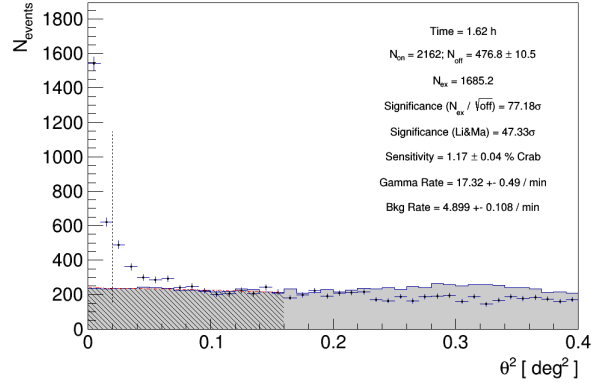

Fig 27. Distribution of the squared angular distance θ^2 considering a low energy range (LE), for events in the direction of Crab Nebula (blue points) and normalized off-source events (grey histogram) for data taken on the 29th of September 2016
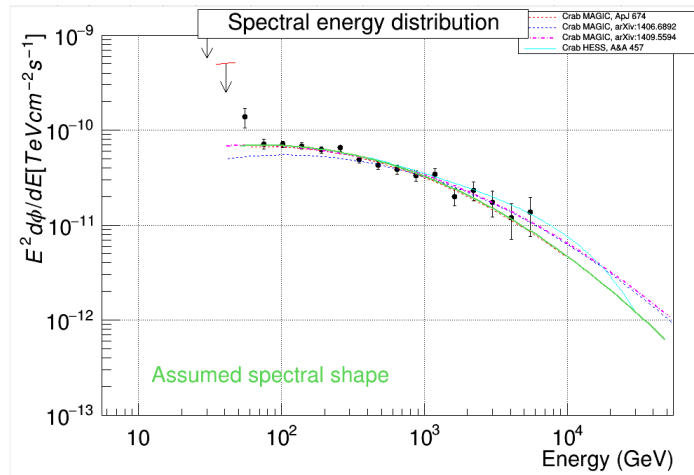

Fig 28. SED of the Crab Nebula as measured by MAGIC, on the 29th of September 2016. The black dots represents the spectrum while the upper limits are shown as black arrows. The best fit is represented by the green line. For comparison purposes, the results from previous studies from the bibliography are also plotted in other coloured lines.

Once we have already finished with this part of the analysis, the next section will tell the procedure followed for the analysis of the HE range for the emission of OT 081.

3.2   Analysis of Fermi data

3.2.1   Spectral analysis

The Fermi analysis is based on a likelihood fit. We will compare the observations with a XML model that includes all the sources present in the FoV and also diffuse emission models. This output XML model that we will create is giving the best result of a spectral fit for each of the sources considered.

Calibrated data from Fermi-LAT are available online and they can be downloaded from the Extract Lat data server[3]. The analysis can be done by using the software Fermi Science Tools from NASA's Heasarc[4], which is specifically designed for the data reduction in the HE range as observed by Fermi.

As the Fermi-LAT works in survey mode, we choose the specific data in accordance with the dates (UTC) when the flare was detected with MAGIC (+-12 hours before and after this time). We selected data with a radius of 20 degrees from OT 081 and covering an energy range between 100 MeV and 50000 MeV. We had to put the coordinates of our source in degrees, the radius of the search and the wanted energy range in MeV as required inputs.

The data extraction provides two kinds of files: event files, where the photon position and energy are given (L*_PH*.fits) and a spacecraft data file, which gives the information of the spacecraft at the moment of the observations (L*_SC*.fits). There is another type of files needed that correspond to background models for diffuse sources. So the background models called gll_iem_v06.fits and iso_P8R2_SOURCE_V6_v06.txt [5] were downloaded and used for the analysis.

As we said, the Fermi analysis is performed with a likelihood algorithm. It can be done by following two possible options: Binned and/or Unbinned Likelihood Analysis. The Unbinned uses all the energy available of each event, while the Binned Analysis joins this energy into bins to reduce the execution time, due to this type of analysis is thought to work with large amounts of data as Fermi usually offers. We chose the Unbinned tutorial [6]because the amount of data we want to analyse was small enough (only one day of observing time).

Next, we give a description of each of the steps followed in the tutorial for the source analysis and the obtained results.

---

[3]https://fermi.gsfc.nasa.gov/cgi-bin/ssc/LAT/LATDataQuery.cgi
[4]Downloaded from: https://fermi.gsfc.nasa.gov/ssc/data/analysis/software/
[5]Downloaded from: https://fermi.gsfc.nasa.gov/ssc/data/access/lat/BackgroundModels.html
[6]https://fermi.gsfc.nasa.gov/ssc/data/analysis/scitools/likelihood_tutorial.html

1. Data selection: gtselect, gtmktime, gtvcut

First of all, we perform selection cuts on the event data files extracted from the Fermi-LAT database, applying the tool gtselect. This selection involves time (interval of the observation time chosen), energy (range of energies chosen for the observations) and event class cut types. Different event classes are available but we only keep the source class events.

After that, we select good time intervals (GTIs) using the tool gtmktime. They consist of those intervals in which the satellite was working in standard data taking mode. GTIs are extracted from the information given by the spacecraft file.

Finally, we can check the cuts applied to the data using the gtvcut tool.

2. Counts map: gtbin

Now, it is interesting to create a count map of the region of interest (ROI) in order to visualize the photon distribution within the FoV and identify clusters which are expected from the sources in this field. To do this, the gtbin tool with the option CMAP is applied after the data selection. The resulting count map plotted by ds9 is given in Figure 29.
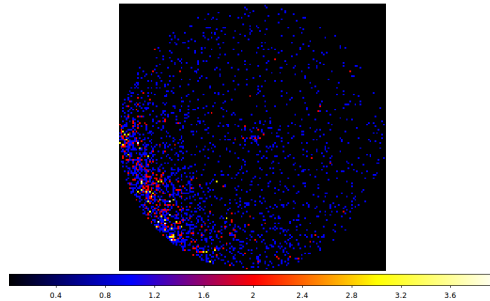

Fig 29. Counts map of the OT 081 region, opened with ds9 tool.

3. Exposure map: gtlcube, gtexpmap

This next step generates an exposure map. The likelihood algorithm uses a type of exposure that consist of doing the integral of the total response over the full ROI. We need to apply two steps to calculate the exposure map:

- **3.1 Livetime cube**

We want to calculate how much time the spacecraft was covering a certain position in the sky. To do this estimation, the tool gtltcube uses the spacecraft pointing history file along with the time range and GTI selections in the event file, to perform livetime cubes which cover the full sky. It is also important to take into account that the LAT instrument response functions depend on the angle between the direction to a source and the instrument z-axis (also called off-axis angle).

- **3.2 Exposure map**

To be able to obtain our source model in future steps, it is required the computation of the predicted number of photons within a given ROI for the sources that have been observed. However, this parameter can be only determined if an exposure map has already been calculated. The gtexpmap tool generates this exposure map by taking as inputs the livetime cube, the spacecraft file and the results after the data selection.

Among the input parameter options, it is important to choose a slightly large radius of the source region with respect to the ROI we are analysing. The Fermi PSF is much worse than traditional ground-telescopes, reaching up to $\sim 10°$ at ~ 100 MeV (see Figure 30). That is why we need to cover a broader region to ensure that photons coming from other sources outside the ROI are taken into account. This implies a source region, centered on the ROI, with a radius that is larger than the ROI radius by at least one PSF length scale. Taking into account that our source is a point-like source, a total radius of 30 degrees was chosen, because an extension of 10 degrees (the PSF value) is good enough for this purpose.
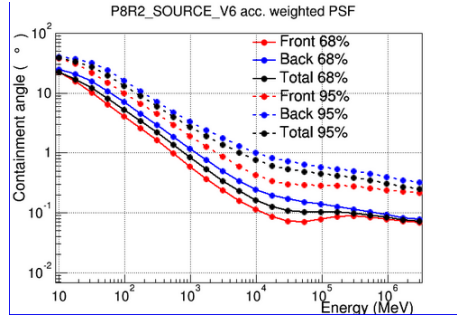

Fig 30. Graph of the contribution of the containment angles (68% and 95 %) for the weighted PSF of Fermi-LAT.

4. Source model XML file: make3FGLxml.py

As Fermi-LAT works in a survey mode, it observes many sources in a certain sky region. Therefore, it is needed a XML model to account all these sources that are present in the same FoV as our source of interest. This XML model will be used later in the analysis by the likelihood fit to be compared with the photon distribution within the FoV.

To generate this XML model first, it is executed a python script (make3FGLxml.py)[7] that contains information of all the sources and also the background model files. The accounted sources are retrieved from the Fermi-LAT 3FGL Catalog[8]. This corresponds to the third full catalog during 4 years of observation time, with data retrieved from the point sources found in HE during the surveys. [9].

---

[7]Downloaded from: https://fermi.gsfc.nasa.gov/ssc/data/analysis/user/
[8]Retrieved from: https://fermi.gsfc.nasa.gov/ssc/data/access/lat/4yr_catalog/
[9] LAT 4-year Point Source catalog

In addition, if we have extended sources in the model (apart from the background models), some templates are needed to put as input inside the script. These extended source templates can be downloaded from the LAT server [10].

The input XML model created accounts for all the sources within a region of 30 degrees, in which our source (3FGL J1751.5+0939) is well described by power-law fit spectral type as reported in the 3FGL catalog. Within this XML model, some parameters will be fixed and others will be set as free. For the sources located up to 20 degrees from our source, all their spectral parameters are set as free (flux and spectral index). However, for the sources placed between 20 and 30 degrees from our source, the flux is set as free but the spectral index is fixed using the value given by the 3FGL catalog.

5. Diffuse source responses: gtdiffrsp

The Unbinned Likelihood function is defined in terms of the expected photon distribution for a given source model. That distribution is the convolution of the source model with the instrument response. The contribution associated with an individual photon is computed as the integral of the source model with the instrument response evaluated at the observed photon direction, energy and arrival time. For point sources, the spatial component is easy to compute, although for diffuse sources the computation is much more intensive since it must be performed over the whole sky. This is the reason why it is more convenient to precompute these quantities.

The gtdiffrsp tool will perform these integrations (called as diffuse responses). Since the diffuse response is linked to the instrument response function (IRF), we chose the IRF called P8R2_SOURCE_V6 correctly according to the selection of events we have made.
We included the spacecraft and photon files as inputs adding as well the source model XML file we have obtained in the previous step. The result is added as an additional column to the event file.

6. Likelihood fit: gtlike

The likelihood fit is carried out using the gtlike task. During the likelihood analysis, the spectral fit for each source in the input XML model is calculated. For the parameters estimation, we used an optimizer called NEWMINUIT, which usually provides more accurate results even though the convergence of the results sometimes takes more time than other optimizers.
To run gtlike we used all the outputs from the previous steps. Before executing this task, we fixed the spectral index of the fit and set free the flux in the case of OT 081. The parameters of the fit, the integrated flux and the TS value, all for each point and diffuse sources, make up the information given by this XML output model. The results in the case of OT 081 are shown in Table 5.

---

[10] Extended Source template archive (https://fermi.gsfc.nasa.gov/ssc/data/access/lat/4yr_catalog/)

Source Name	Type of fit	Γ	$f\,(ph{\cdot}cm^{-2}s^{-1})$	TS value
3FGL J1751.5+0939	Power-Law	2.15 ±0.07	$8.423{\cdot}10^{-7}$	72.75 (8.53σ)

Table 5. Results from the fit with the tool gtlike, for the source OT 081. The significance of the detection is given within the brackets of the fifth column, since its value corresponds approximately to the square root of the TS value.

7. Building the Fermi SED: likeSED.py

To build the SED we use a specific tool (SED_scripts_*.tgz)[11] which contains macros that help the Fermi Science Tools software to produce spectral plots of LAT sources. We run a likelihood analysis for individual energy bands so we are able to calculate the flux in each band plotted with the maximum likelihood model fit.

Within the set of macros, we used specifically the likeSED.py macro, which is made for the Unbinned Likelihood analysis method. We created a script in which the likeSED.py macro was called so its functions can be imported.

According to these functions, some parameters have to be fixed. All the needed inputs are: the photon event file obtained after the data selection, the spacecraft file, the exposure map, the livetime cube and the instrument response function (IRF) used (P8R2_SOURCE_V6). In addition, the likelihood result for the entire energy range and the optimizer applied (NEWMINUIT) are required. Finally, we also put the name of the source given in the output XML model (3FGL J1751.5+0939) and the optional input of nbin, which is basically a tool that let us to choose the number of energy bins we want. In Figure 31, we can see the plots we have used to analyse the results, for a nbin = 7.
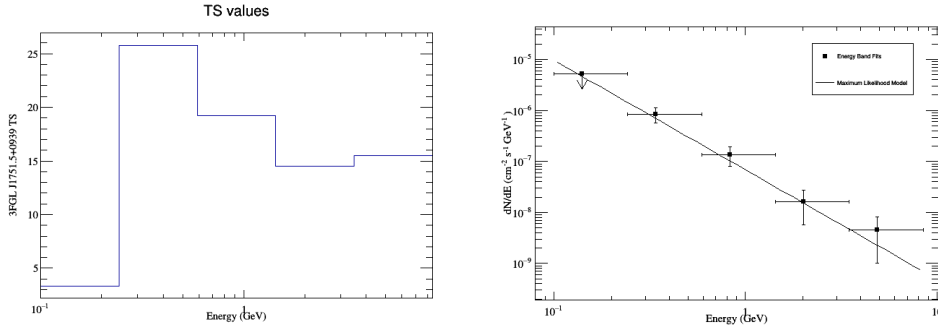
Fig 31. Developed plots for the case of a number of energy bins equal to 7. Left: Distribution plot of the TS values. Right: Source spectrum fitted to a power law, with an upper limit represented by the arrow.

The final SED of Fermi-LAT data from our source is plotted in Figure 32. This allows us to construct another additional part of the MW SED that we will check in section (4.2).

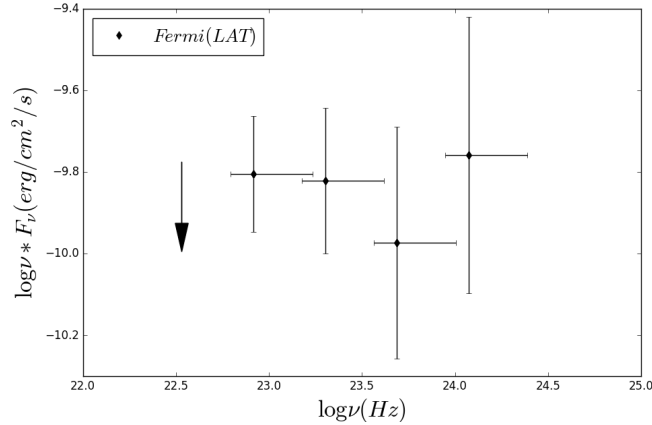[11] Downloaded from: https://fermi.gsfc.nasa.gov/ssc/data/analysis/user/

Fig 32. SED of OT 081 above 100 MeV of the Fermi-LAT data, during the flare state of this source. The arrow
represents an upper limit to the total values.

3.2.2   Light-curve analysis

If we follow the same procedure we have done in the previous analysis but covering a large set of dates,
then we can build a light curve for the Fermi-LAT data. This is very time-consuming so it was run
by an automatic script developed by my tutor. A text file containing the data of time, flux, spectral
index and TS value for this particular source was acquired. I made a script in Python programming
language to be able to plot all the results, which can be finally found in Figure 33.
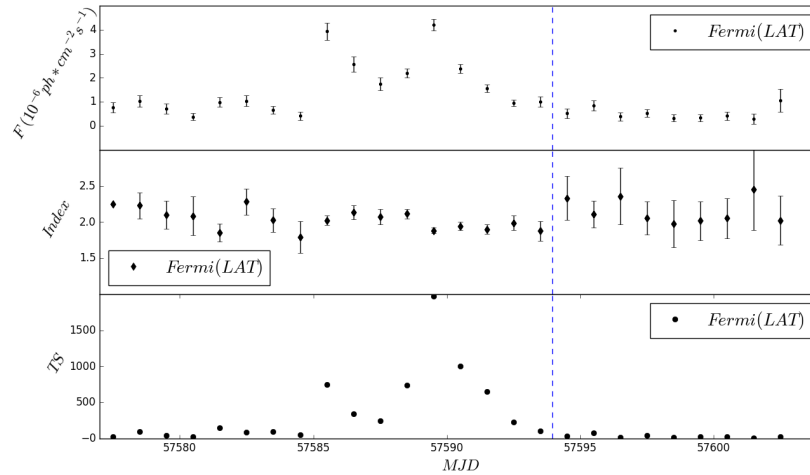
Fig 33. Light curve of OT 081 of the Fermi-LAT data for E>100 MeV in the upper panel. The middle panel
represents the photon index and the lower panel shows the test statistic values, both of the LAT data of OT 081. The
dashed blue line represents the time when the flare was observed by MAGIC, on the 25th of July 2016.

As we can see, I plotted a vertical dashed line indicating the day when the flare was detected by
MAGIC. It can be noticed that the flare started before that detection. MAGIC could not observe
before due to strong moon light conditions and bad weather. As detected by Fermi-LAT, on the 25th
of July 2016 the flux was decreasing to lower values but there was enough signal in the HE range.

The spectral index gets harder when brighter, as we can see in the results by comparing the two first subplots. In order to see better this correlation, we plotted the spectral index vs. the flux, as it is shown in Figure 34.
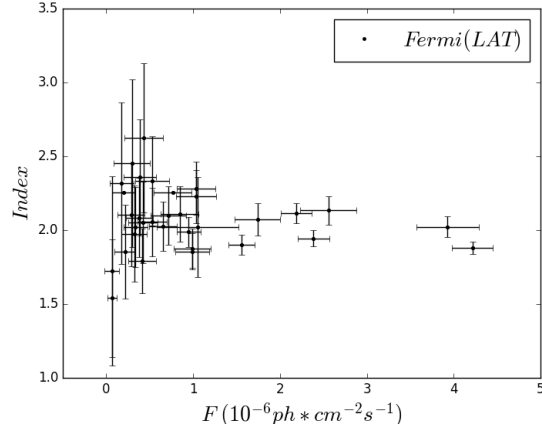

Fig 34. Correlation plot between the spectral index and the integral flux from Fermi-LAT data of the source OT 081.

After some calculations, this correlation results significative, with a Pearson coefficient of 0.59 (3.4σ). Besides, in Figure 33 it can be seen that Fermi-LAT observed a flare with intravariability (denoted as two bumps in the curve) in a short period of time (between MJD $\sim$57585 and $\sim$57590) and with a considerable increase in flux with respect to the low-state ($F_{flare}/F_{lowstate} \sim 4.12$). These two peaks can be easily seen in the flux as well as in the TS value.

This analysis together with the MAGIC analysis will be part of the total MW SED and the MC LC. The final results along with additional measurements in different frequencies of the spectrum, are described in the sext section.

4   Description of the results

As discussed before, MW studies of this particular source were encouraged due to the appearance of a flare, which was observed by MAGIC, Fermi-LAT, Swift and also in optical. In addition, possible correlations between different energy bands of the same event can be studied as well to understand better the physical processes that take place within the jet of this source.

In this section, we have joined the results of both MAGIC and Fermi analyses and also we have collected data from other instruments observing at different energy ranges. Furthermore, by means of the building of the MW SED, we are able to study it within the context of physically motivated jet emission models. Since OT 081 is classified as a BL Lac object, the MW SED modelling will be performed using the standard SSC models, which are typically used for this kind of sources. Those observations taken from other telescopes are detailed in Table 6:

INSTRUMENT	ENERGY BAND	ν_{eff} (GHz)	MJD MIN.	MJD MAX.
OVRO	Radio	15	54473.7	57820.5
Metsähovi	Radio	37	57392.4	57753.4
IRAM (3 mm)	Radio	100	57217.5	57677.5
IRAM (1 mm)	Radio	300	57217.5	57677.5
RINGO (camera d)	Optical	$3.39 \cdot 10^5$	57090.2	57662.8
RINGO (camera f)	Optical	$4.25 \cdot 10^5$	57090.2	57662.8
RINGO (camera e)	Optical	$6.06 \cdot 10^5$	57090.2	57662.8
KVA (R band)	Optical	$4.56 \cdot 10^5$	55446.9	57909.1
XRT (2-10 keV)	X-rays	$4.83 \cdot 10^8 - 2.42 \cdot 10^9$	54157.7	57596.8
XRT (0.3-10 keV)	X-rays	$7.25 \cdot 10^7 - 2.42 \cdot 10^9$	54157.7	57596.8
XRT (index)	X-rays	-	54157.7	57596.8
UVOT (filter V)	X-rays	$5.49 \cdot 10^5$	54157.8	57595.8
UVOT (filter B)	X-rays	$6.83 \cdot 10^5$	54157.8	57595.8
UVOT (filter U)	X-rays	$8.66 \cdot 10^5$	54157.8	57595.8
UVOT (filter UVW1)	X-rays	$1.15 \cdot 10^6$	54157.8	57595.8
UVOT (filter UVM2)	X-rays	$1.33 \cdot 10^6$	54157.8	57595.8
UVOT (filter UVW2)	X-rays	$1.56 \cdot 10^6$	54157.8	57595.8

Table 6. Observations of OT 081 from frequencies between radio and X-rays. The first and second columns provide the name and energy bands of the corresponding instruments. The third column gives the effective frequency of each observation with repect to the telescope used, in GHz. In the two last columns is given the time interval of each observation (minimum and maximum time achieved), in Modified Julian Day (MJD) units.

We can see a wide range of measures that covers from radio frequencies to X-rays. This way, it would give a greater coverage of the MW SED. Some other kind of data as spectral index values are also useful to visualize the change of our flare in the MW LC.

In the next sections, the MW LC and the MW SED for all of the data available are plotted and analysed. The plots have been obtained using the Python programming language and two scripts: one for the LC and other for the SED extraction.

4.1   Multi-wavelength Light Curve

The MW Light Curve shows the evolution of the flux at each energy band with respect to the time of each observation, given in Modified Julian Days (MJD) units. A MJD can be easily converted to Julian Day (JD) units by the following formula: MJD = JD − 2400000.5
However, the conversion from MJD to UTC time (or backwards) is more tedious, so it has been done with the time converter tool[12] and with the astropy.time package available in Python.

In addition, different instruments use unalike time convenctions. For the specific cases of Swift and

---

[12]xTime – A Date/Time Conversion Utility: https://heasarc.gsfc.nasa.gov/cgi-bin/Tools/xTime/xTime.pl

Fermi observations, the time used by the interface of their softwares was given in Mission Elapsed Time (MET) units. So we want to convert these units to the same MJD units as the other telescopes data.

All of them were converted from MET to MJD applying the following formula: MJD = MET/86400 (s) + MJDREFI + MJDREFF. Where these needed values are already fixed and correspond to: MJDREFI = 51910, MJDREFF = $7.42\widehat{8703}\cdot10^{-4}$ and the factor 86400, which are the seconds contained in a day (24 hours).

The final MW LC plot covering a MJD from ∼54000 to ∼58000 is given in the Appendix A (see Figure A1). There we can see a dashed blue vertical line, which represents the day when MAGIC measured the flare. It can also be noticed that all the energy bands present an increase of the flux, clearly seen as a peak at this time. However, as we do not have long-term data from some of the observations (as Fermi-LAT or XRT), we cannot ensure the flare detection in all the frequencies.

In order to focus deeply on the VHE flare, we represented the flare plot (zoom over that region) where the MJD limits are changed to a closer region, including the full flare detected in the HE band by Fermi-LAT . This can be seen in next Figure 35.
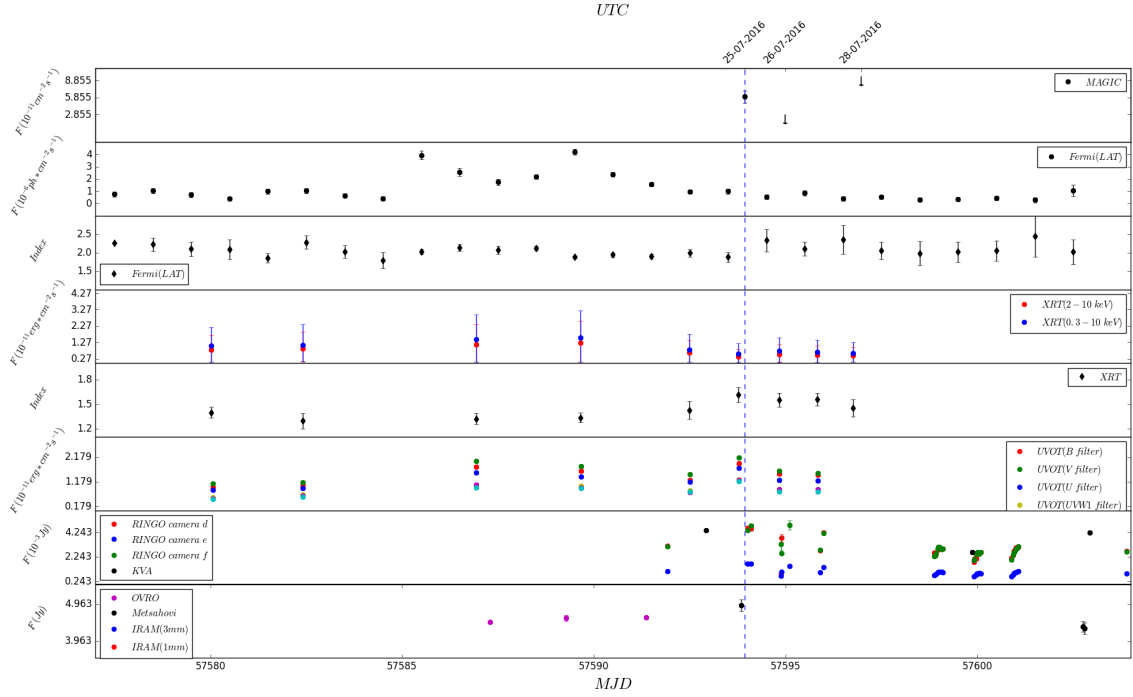

Fig 35. Bounded area of the light curve of OT 081 closer to the time interval when the flare was detected, from radio up to the VHE range. The dashed blue line represents the time when the flare was observed by MAGIC, on the 25th of July 2016.

Now, the three days of MAGIC observations are easily distinguished (the two last days as 95 % U.L.) and the dashed line is set again over the MAGIC detection. The first thing to take into account is that Fermi-LAT observed this flare before than MAGIC, so MAGIC detected the flare already in the decay phase as we commented in subsection 3.2.2. In addition, X-ray observations show an increase of

the flux also before that date, and then the flux lowers and stabilizes ($F_{flare}/F_{lowstate} \sim 2.26$).

If we pay attention to the Figure A1, we will check that for optical and radio frequencies, the flare last more than the MJD interval plotted here in Figure 35. So the change in flux for this zoomed plot is almost imperceptible. The flux rates we calculated from Figure 35 are: in the case of the optical, the observed flux rate is $F_{flare}/F_{lowstate} \sim 2.47$, while for the radio emisison is $F_{flare}/F_{lowstate} \sim 1.14$. For this last energy band we do not see almost any change in the emission of this source. However, this is not strange because it is already known that the radio emission from blazars usually comes from outer parts of the jet, and not from the same region as the other frequencies due to self-absorption.

A MW SED will be built from the dates close in time to the MAGIC detection to get a simultaneous SED. We can see that UVOT, RINGO, KVA, Metsähovi and OVRO have near measurements to this flare detection. These points will be taken and represented in the MW SED with the other MAGIC and Fermi-LAT data. In the case of XRT measurements, we extracted and analysed the data from the Swift database (which also works in survey mode). Swift detected this flare just 4 hours and 10 minutes before MAGIC did, so we used the SED obtained from these observations to plot it in the MW SED. As the effective frequencies for each observation is already given in Table 6, we are able to plot the SED for the energy (frequency) of each measurement chosen. In Table 7, it is shown this selection of data, along with the time difference with respect to the flare detection of MAGIC.

INSTRUMENT	ENERGY BAND	$\nu \cdot F \, (erg \cdot cm^2 s^{-1})$	$\pm \triangle \, (\nu \cdot F)$	MJD	$\triangle t_{obs-MAGIC}$
OVRO	Radio	$6.901 \cdot 10^{-13}$	$5.313 \cdot 10^{-33}$	57591.3	62 hours before
Metsähovi	Radio	$1.824 \cdot 10^{-12}$	$5.701 \cdot 10^{-32}$	57593.8	2 hours y 12 min before
RINGO (camera d)	Optical	$1.560 \cdot 10^{-11}$	$4.376 \cdot 10^{-13}$	57594.0	1 hour and 36 min after
RINGO (camera f)	Optical	$1.878 \cdot 10^{-11}$	$3.923 \cdot 10^{-13}$	57594.0	1 hour and 36 min after
RINGO (camera e)	Optical	$1.011 \cdot 10^{-11}$	$1.720 \cdot 10^{-13}$	57594.0	1 hour and 36 min after
KVA (R band)	Optical	$2.007 \cdot 10^{-11}$	$3.330 \cdot 10^{-13}$	57592.9	24 hours and 25 min before
UVOT (filter V)	X-rays	$2.162 \cdot 10^{-11}$	$6.255 \cdot 10^{-13}$	57593.8	3 hours and 53 min before
UVOT (filter B)	X-rays	$1.912 \cdot 10^{-11}$	$6.353 \cdot 10^{-13}$	57593.8	3 hours and 53 min before
UVOT (filter U)	X-rays	$1.723 \cdot 10^{-11}$	$5.714 \cdot 10^{-13}$	57593.8	3 hours and 53 min before
UVOT (filter UVW1)	X-rays	$1.258 \cdot 10^{-11}$	$4.962 \cdot 10^{-13}$	57593.8	3 hours and 53 min before
UVOT (filter UVM2)	X-rays	$1.242 \cdot 10^{-11}$	$6.679 \cdot 10^{-13}$	57593.8	3 hours and 53 min before
UVOT (filter UVW2)	X-rays	$1.183 \cdot 10^{-11}$	$4.512 \cdot 10^{-13}$	57593.8	3 hours and 53 min before

Table 7. Observations of OT 081 from frequencies between radio and X-rays, closer to the day of the MAGIC detection. The first and second columns provide the name and energy bands of the corresponding instruments. The third and fourth columns give the frequency multiplied by the flux, according to the SED units and its error. In the two last columns is given the time of the flare observations in MJD units and the time difference between these observations and the detection by MAGIC.

4.2   Multi-wavelentgh SED

In this case, we had to fix the same units for the flux to all the multi-frequency data points. Here, we have plotted the observed flux multiplied by the frequency with respect to the frequency, both axis given in logarithms. We can see it represented in Figure 36.
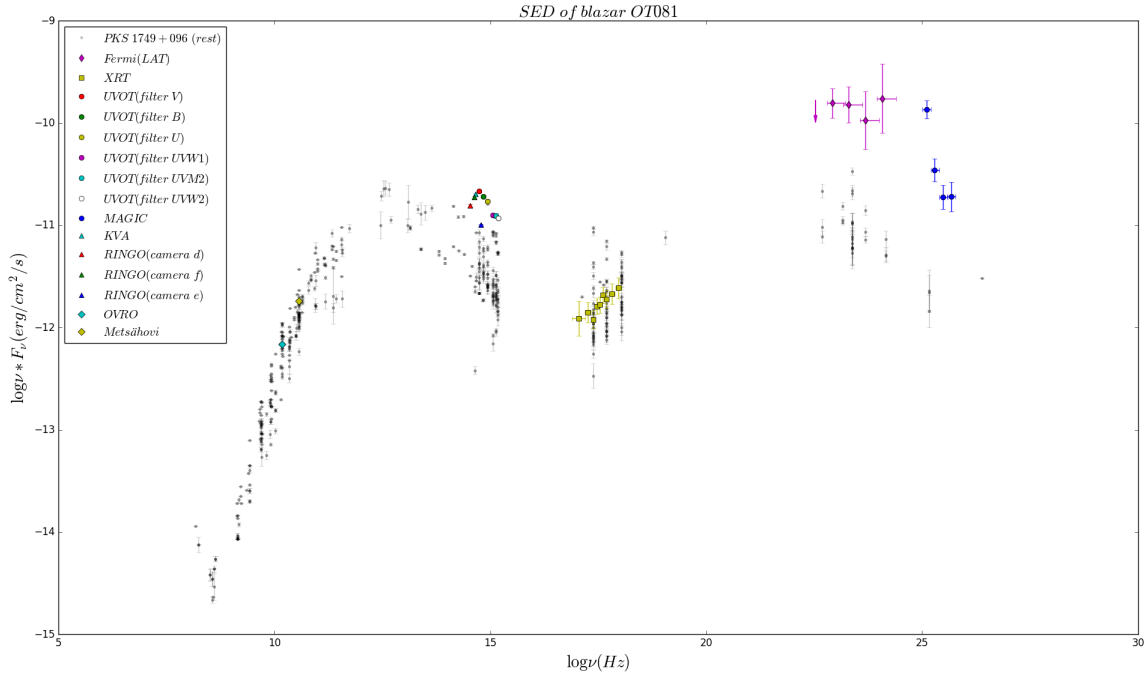

Fig 36. SED of OT 081, from radio frequencies up to the VHE range. The grey dots represent the quiescent state of the source, while the other markers are the different measurements of the high state from the telescopes detailed in the legend.

For reference, we have plotted in grey the available MW archival data for comparison purposes with respect to the quiescent state and previous flaring states (when the flares appear, we call it high state). The archival data were retrieved from the online tool called SED builder[13]. In that webpage, there are MW data from sources at different energy bands. Therefore, we looked for the name of OT081 to download the text file with the available data.

The observations and their corresponding errors during the flaring event we are studying in this work are represented by the color markers in Figure 36 (some errors were quite small and there are not perceptible in the plot).

If we compare the low state and the high states at first sight, we can see that they differ in some characteristics:

- When comparing the flaring state with the archival data we notice that there is a global rise of the whole data to larger values of flux, which is the first characteristic change in these types of sources

---

[13]https://tools.ssdc.asi.it/

when they are emitting during a flare event. The amount of flux that changes will not be the same for all the energy bands, but higher in the case of the HE and VHE ranges or smaller for X-rays and optical. Actually, we can check that the radio emission has not changed its flux between the low and the high states, as we mentioned before with the MW LC.

- A second visible difference is a general shift of the whole SED in its high state to higher energies, that is, to the right part of the x axis. So it seems that both peaks are changing their position in the course of a flare. However, this particular characteristic is clearer for the second peak than for the first one, since for the Synchrotron bump we do not have enough data to make a good comparison.

- The third feature is the most noticeable, and is related to the ratio between the first and the second peak of the SED. While the low-state data give a similar flux for both peaks (almost the same value for the y-axis), the high state presents an evident increase of the second peak flux. However, the observed ratio between the peaks for the high state is not usual for BL Lacs types. Instead, it is a characteristic feature of the FSRQ blazar types (already discussed in section 1.3 with the blazar sequence plot) originated by the influence of an additional External Compton field. So this source seems to share some intrinsic behaviour between the FSRQ and BL Lac object types.

The BL Lac objects are dinamical sources that can change from its quiescent to high state. Therefore, the classification given by the blazar sequence can be slightly modified when the source changes from the low to the high state. In order to verify this kind of difference, we used the so-called Compton Dominance plot (Finke, 2011). This plot represents the ratio between the fluxes of the IC and the Synchrotron peaks as a function of the synchrotron frequency for the first peak. It illustrates how dominant is the IC scattering with respect to the Synchrotron process, according to measurement results from different types of blazars (see Figure 37).
According to the MW SED plot, the maximum flux of both bumps and their peak frequencies and the calculation of the Compton Dominance, for the low state and the high state, are detailed in Table 8.

Source state	$F_{peak}^{Syn}(erg \cdot cm^{-2} s^{-1})$	$\nu_{peak}^{Syn}(Hz)$	$F_{peak}^{IC}(erg \cdot cm^{-2} s^{-1})$	$\nu_{peak}^{IC}(Hz)$	$F_{peak}^{IC}/F_{peak}^{Syn}$
Low State (LS)	$1.44 \cdot 10^{-11}$	$2.10 \cdot 10^{13}$	$2.04 \cdot 10^{-11}$	$2.42 \cdot 10^{23}$	1.418
High State (HS)	$1.91 \cdot 10^{-11}$	$6.83 \cdot 10^{14}$	$1.74 \cdot 10^{-10}$	$1.18 \cdot 10^{24}$	9.103

Table 8. Values of the flux and frequencies of the Synchrotron and Inverse Compton peaks, and flux ratios between the second and the first peak of the SED (also called Compton dominance), for the low and high states of OT 081.

By using the estimated ratios for the low and the high states given in Table 8, we can draw these results over the Compton Dominance plot obtained by Justin D. Finke in order to see the classification difference between both states (see Figure 37).
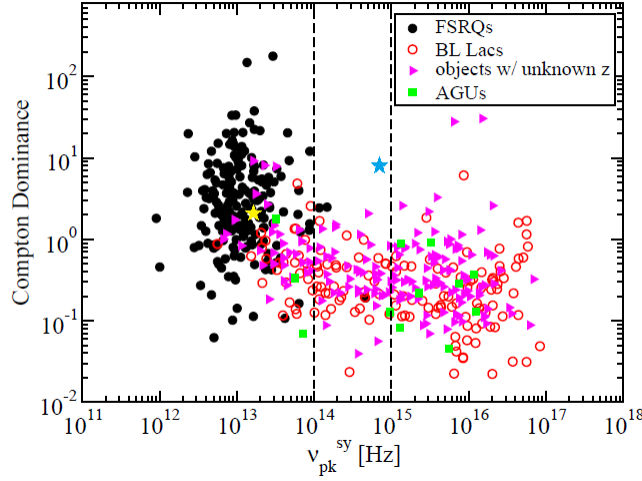
Fig 37. Compton Dominance (i.e. $F^{IC}_{peak}/F^{Syn}_{peak}$) versus peak Synchrotron frequency (Finke, 2011). The data described in the legend correspond to a sample of blazars obtained from the Second Catalog of Active Galactic Nuclei (AGN) from the Fermi Large Area Telescope (LAT). Filled circles represent FSRQs, empty circles represent BL Lacs, filled green squares represent objects which have an ambiguous classification and rightward-pointing triangles represent BL Lacs with unknown redshifts. Dashed lines indicate the boundary between HSPs and ISPs ($\nu^{Syn}_{peak} = 10^{15}$Hz) and between ISPs and LSPs ($\nu^{Syn}_{peak}= 10^{14}$Hz). The data from OT 081 is plotted as yellow and blue filled stars, for the LS and HS respectively, taking into account the information given by Table 8.

The original Compton Dominance plot (Finke, 2011) have been made using a sample of blazars from the Second Catalog of Active Galactic Nuclei (AGN) from the Fermi Large Area Telescope (LAT)[14] which contains measurements along two years of scientific operation. Since it integrates the data during a long period of time, this sample can be representative of the sources in a quiescent state. If we focus on our results, which are represented as yellow and blue stars symbols in Figure 37, we can see the classification wheter we consider the low or the high state of our source. In the case of the low state (yellow star) our source is located near the FSRQs zone although there are also some BL Lacs around this part of the plot. Its Compton Dominance is not particulary high, so in that sense it looks like more to a BL Lac object type according to the distribution shown in the plot. For the high state (blue star), the Compton Dominance is strong so it is more like to the levels reached by the FSRQs. However, due to its Synchrotron peak frequency, the source is located in the zone where the BL Lacs are more grouped. We can conclude that the classification of our source could be changing betwen a FSRQ to a LBL class depending on the features considered and always in terms of the source state. This thin line that distinguishes both classes is still quite complicated to explain, so deeper studies for these types of blazars should be carried out.

In the next part of this section, we will see the theoretical emission model we have applied. There, we will discuss the previous question and the possible explanations according to the model we have applied.

---

[14]2LAC catalog of AGNs detected by the Fermi-LAT (Ackermann et al. 2011)

4.3   OT 081 jet emission: SSC modelling

Once the MW SED of our source is built, we are able to apply a theoretical model to the emission coming from the jet. The BL Lac objects are typically well described by the leptonic Synchrotron-Self Compton (SSC) model. Within the two peak distribution of the SED, the first bump is explained by the Synchrotron emission of the electrons moving along the magnetic field lines inside the jet, while the second bump is caused by the Inverse Compton (IC) scattering. There are two types of mechanisms that can originate this IC emission: the SSC process (where the same population of electrons that produce Synchrotron emission are interacting with the Synchrotron photons) or the influence of an External Compton field. The influence of one or the other depends on the type of blazar where this emission is happening. For BL Lacs, external photon fields are not typically present, so it does not play a key role in the jet emission of the second peak and the SSC mechanism dominates.

In order to explain the SSC model, one of the key parameters is the electron population, which is going to be the same for the two bump Synchrotron and IC processes. This electron distribution can be assumed as a broken power law, whose parameters are detailed in Equation (5).

$$N\left(\gamma\right) = \begin{cases} K\gamma^{-n_1} & if \quad \gamma_{min} < \gamma < \gamma_b \\ K\gamma^{-n_2} & if \quad \gamma_b < \gamma < \gamma_{max} \end{cases} \tag{5}$$

Where the γ's are the Lorentz factors of the electrons: γ on the rest frame of the jet, γ_{min} the minimum value, γ_b the break value and γ_{max} the maximum value; the n_1 and n_2 are the spectral indices of this electron distribution before and after the break, respectively; and K is a normalization constant.

Moreover, the size of the emitting region in the jet is also taken into account, according to standard one-zone models. A spherical distribution with radius R is assumed, being this size comparable to the jet cross section.
It will be also needed the magnetic field intensity (B) and the electron density (n_e), as well as the redshift of our source (z) and the Doppler factor (δ). The Doppler factor is related with the velocity of the jet and the angle between the velocity vector and the line-of-sight to the observer. It is defined when the jet velocity is closer to the speed of light and some effects as the light aberration or the arrival time contraction occur.

Besides, the radius of the emitting region will be calculated using the Casuality relation, given below in Equation (6).

$$R < \frac{c \cdot t \cdot \delta}{(1+z)} \tag{6}$$

Where c is the speed of light in the vacuum in cm/s, t is the variability timescale of the observation in seconds, z is the redshift of the source and δ is the Doppler factor.

It is important to know which parameters are more or less fixed and cannot change drastically because of the restrictions to the SSC model. For example, the redshift of OT 081 is z = 0.322 and the variability timescale can be taken as 24 hours according to the timescales in which the flux of the source changes. Besides, the Doppler factor oscillates between 10 and 40 for this type of model (and typically does not exceed over 30). Due to these restrictions, the possible values for the radius of the emitting region will be also bounded in terms of these three parameters, as seen in Equation (6).

When we were changing the parameters to apply them to the model, we realized that the intensity of the magnetic field had to be truly small. Otherwise the Synchrotron emission is overproduced, and the entire fit would never resolved the two-peaked structure of the SED. By testing many possible configurations, we found two models that approach to a good fit of the results (see Table 9). The resulting plots of both test models are shown in Figure 38, where the high state is given in red coloured dots and the final fit is represented by the black solid line. As seen in Figure 38, the radio emission of our source given by OVRO and Metsähovi measurements is not fitted. This is because the radio emission is not believed to be formed in the same region of the jet than the other frequencies, but it is suggested to have its contribution at outer parts of the jet.

Model	γ_{min}	γ_b	γ_{max}	n_1	n_2	$B[G]$	$n_e[cm^{-3}]$	$R[cm]$	δ	z
A	1	5	$7 \cdot 10^4$	2.17	2.17	0.0075	$1.1 \cdot 10^5$	$6.4 \cdot 10^{16}$	26	0.322
B	350	$2.6 \cdot 10^4$	10^5	2.17	3.15	0.007	$1.1 \cdot 10^5$	$6.4 \cdot 10^{16}$	27	0.322

Table 9. Input parameters for the best emission SSC models obtained. γ_{min} , γ_b and γ_{max} are the minimum, break and maximum Lorentz factors of the electron population, respectively, while n_1 and n_2 denote the low and high energy slopes of the broken power-law of the electron distribution. The magnetic field is represented by B, the electron density is given by n_e, the radius of the emission region by R, δ is the Doppler factor chosen and z is the source redshift.
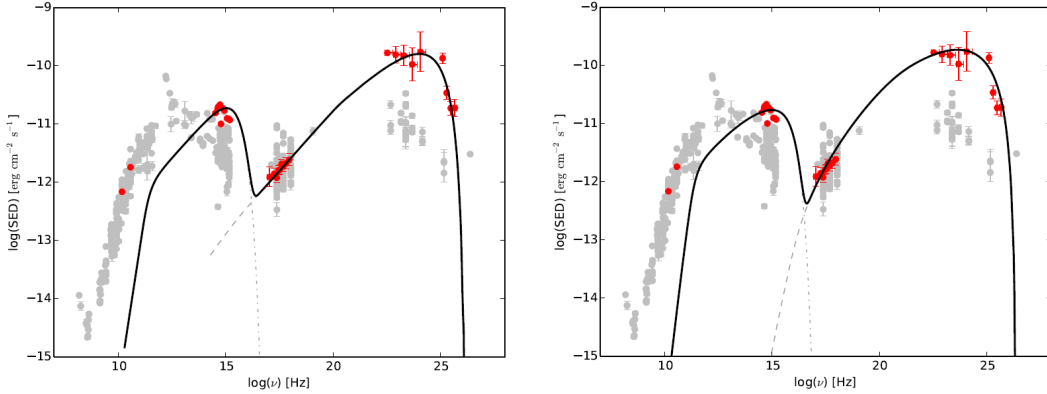

Fig 38. Left: SED fit to the high state by the SSC model A. Right: SED fit to the high state by the SSC model B. The best fit is represented by the black solid line. The low state data are plotted as grey points and the high state data as the red points.

The SSC models successfully reproduce the SED of HBLs but have difficulties in the case of LBLs. Within our parameters, we wanted to reach a good deal between the first and the second bump data fits. As it can be seen, the second peak does not get adjusted correctly (mostly to the Fermi measurements) and it maybe indicates that an External Compton field is needed for that case. Our source OT 081

is classified as an LBL, and this type is thought to be able to share features of both FSRQs and BL Lac objects, due to its classification within the blazar sequence. Precisely for this reason, it could be considered the External Compton field as an additional mechanism to the emission by Inverse Compton scattering, as in the case of the FSRQs. However, there is still missing information about the possibility of a transition between these two types of blazars, as there are only two known LBLs nowdays that emit in VHEs (and one of them is our source of study). The TeVCat online catalog for TeV Astronomy (www.tevcat.uchicago.edu) is made for searching the available sources, filtering the information by type. We found these two LBL sources (OT 081 and AP Librae) and plotted them in a Skymap, where the positions are visually intuitive as we can see in Figure 39.
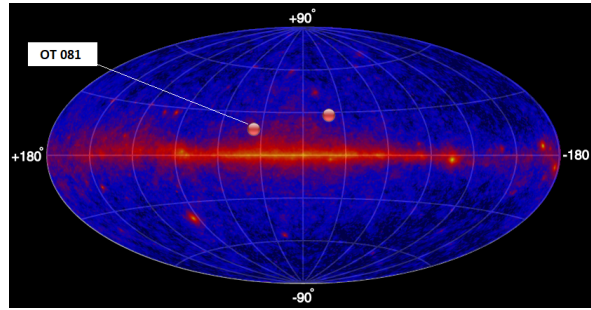

Fig 39. Skymap catalog with the known LBL type sources plotted as red filled circles. Our source OT 081 is located and marked in the skymap. Retrieved from: www.tevcat.uchicago.edu

The AP Librae is a LBL type source at redshift z = 0.049, detected for the first time at HE range by Fermi-LAT (2008-2010) and right after that, at VHEs by the IACT called High Energetic Stereoscopic System (H.E.S.S.) (2010). It was not found any flux variability during the 25 months of Fermi observation. The 11 hours of H.E.S.S. time exposure leads to a detection with significance $\sim 7\sigma$(H.E.S.S. Collaboration, 2015). However, Fermi-LAT detected this source in a high state due to the appearence of two GeV γ-ray flares, one of them on 2011 and the other on 2016. The flux was increased by a factor of ~ 20 and ~ 15, respectively, with respect to its quiescent value. These two notices were published in Astronomer's Telegram webpage (www.astronomerstelergam.org). Other contemporaneous data from different frequencies were also achieved by UVOT, Swift/XRT and RXTE/PCA.

Studies of the AP Librae SED (Fortin et al., 2010), show a very wide high energy component which corresponds to the Inverse Compton scattering emission (almost twice the width than the first bump).This leads to think that the SSC modelling will be challenging. The SSC model applied to a standard one-zone emission, presents serious difficulties to reproduce HE and VHE data (Sanchez et al., 2011). The fit to this second bump is far from a good result, and the proposed solutions could be neither using additional spectral components for these HE and/or VHE observations or considering multiple emission zones. Both results for the AP Librae SED (Fortin et al., 2010), (Sanchez et al., 2011), and the parameters chosen for the SSC model (Sanchez et al., 2011) are shown in Figure 40 and Table 10, respectively.
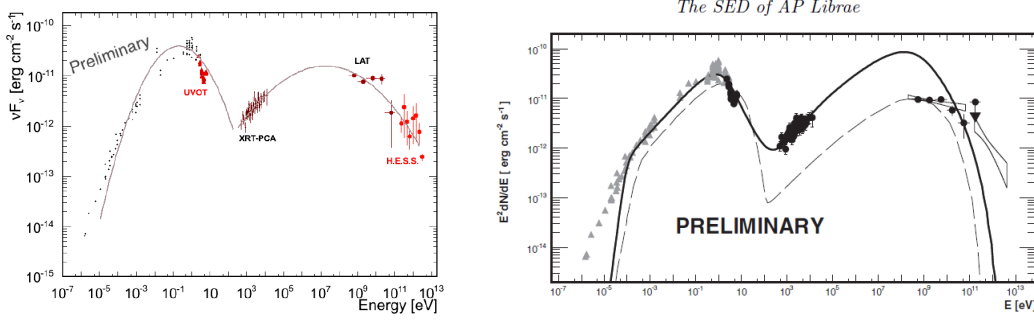
Fig 40. Left: SED of AP Librae. The small black points below the UVOT range are archival data from NED, while the data points above the UVOT range are from contemporaneous Swift/XRT and RXTE/PCA, Fermi- LAT, and H.E.S.S.observations. Each component of the SED was fitted with with a 3rd degree polynomial (Fortin et al., 2010). Right: The time-averaged SED of AP Librae. The solid line is the SSC model (Sanchez et al., 2011) and the dashed line is the model from Tavecchio et al. (2010).

Model	γ_b	n_1	n_2	$B[G]$	δ	z
David Sanchez et al.	$1.4 \cdot 10^4$	2	4.9	0.1	29	0.049

Table 10. Input parameters for the best emission SSC model obtained by David Sanchez et al. for the LBL source AP Librae. γ_b is the break Lorentz factor of the electron population, while n_1 and n_2 denote the low and high energy slopes of the broken power-law of the electron distribution. The magnetic field is represented by B, δ is the Doppler factor chosen and z is the source redshift.

As we can see, these parameters are quite similar to the ones chosen for our SSC model B of OT 081, with the exception of the B [G], which has a higher magnitude in that case and, of course, the redshift of the source. So in the case of the LBLs, we still have the challenge to obtain a well-modelling to the second peak component. That means to test the possible emission processes in charge of creating the highest energy peak of the SED.

5   Conclusions

We have analysed for the first time the blazar OT 081 in the VHE range with the MAGIC telescopes data, taken on July 2016 and with a total observation time of 2.26 hours. A positive detection of the source was obtained for the first day of the flare observation, with a significance in the LE range of 8.41σ. The light curve has been calculated covering all observation time for E > 100 GeV, with an integral flux of $f = (6.0434 \pm 1.05279) \cdot 10^{-11} (ph \cdot cm^{-2} s^{-1})$ for the flare detection date. It was also calculated the SED of the source applying a power-law fit with spectral index $\Gamma = 4.36$. An EBL correction to the SED have been also performed, using the model given by Dominguez et al. (2011). The EBL-corrected spectrum is well fitted by a power-law with a spectral index $\Gamma = 3.66 \pm 0.45$ and a differential flux normalization at 100 GeV of $f_0 = (2.14 \pm 0.24) \cdot 10^{-9} (cm^{-2} s^{-1} TeV^{-1})$.

We have also done the analysis of the source from the Fermi-LAT data in the HE range. For the spectral analysis, an integration of 24 hours centered around the MAGIC observations were selected. An Unbinned Likelihood analysis was performed to obtain the source spectrum, in which the integral

flux and the spectral index values of the power-law fit resulted as $f = 8.423 \cdot 10^{-7} (ph \cdot cm^{-2} s^{-1})$ and $\Gamma = 2.15 \pm 0.07$. It was estimated a significance of the detection according to the results of this fit of 8.53σ. For the light curve estimaton, it was needed an automatic script to apply the analysis to a wider range of observation dates for this flare. It was found an increase of the flux during the flare of approximately four times the flux received when the source was in a quiescent state.

We have built a MW Light Curve and a MW Spectral Energy Distribution, based on the MAGIC and Fermi-LAT results and other data from telescopes working at different energy bands, which also observed this flare near the MAGIC detection. As well as Fermi-LAT, the optical range also measured an increase in flux of approximately 4 times the flux coming from the source in low state, with data retrieved from RINGO and KVA telescopes. We have selected those data closer to the flare detection for each energy band and then plotted the results of the source high state, along with the archive data of its low state for comparison purposes.

Within the MW SED, we have distinguished the main characteristic features of the two bumps of the SED between the source low and high states. A comparison between the Compton Dominance of the low and high states has also been carried out using the study from Justin D. Finke, 2011. We have seen that the classification according to the blazar sequence may change wheter we are observing the source in low state or during a high state. The Compton Dominance value of the high state resulted closer to the ones obtained from a sample of FSRQ blazar type observations, while for the case of the low state, the Compton Dominance value confirms that our source belongs to a region where it can be found both LBL and FSRQ blazar types.

We have modelled the jet emission using a SSC model, being the most proper emission model to choose, according to the classification of the source (BL Lac object). We have found that this model does not fit completely well the MW SED high state data, so an additional External Compton field is encouraged to be introduced into the model in addition to the SSC component. Finally, we have retrieved information from the only other known LBL source, called AP Librae. The modelling of its SED was also challenging for the authors of the study (Sanchez et al., 2011), since they also found problematic issues when trying to apply a SSC model for the jet emission. LBLs can behave as transitional objects between the FSRQ and BL Lac object blazar types, sharing characteristic features between both subclasses. Therefore, as there are still very few known sources of this type, we will need to study deeper these sources one by one when detected and to improve the existing models to be able to known better the origin of the emission in each case.

6   Future perspectives

The next stage is yet to come. The Cherenkov Telescope Array (CTA) Observatory will be the sucessor for the observations in the VHE band and it is considered as the next generation of the ground-based telescopes for γ-ray astronomy. This is an international project and there will be two arrays: CTA-North in La Palma (Canary Islands, Spain) and CTA-South in Arizona (USA).

Three different classes of telescopes: the Small-Sized Telescope (SST), the Medium-Sized Telescope (MST) and the Large-Sized Telescope (LST) are going to cover a broad range of energies (from 20 GeV to 300 TeV) (see Figure 42). MSTs and LSTs will be installed in both emplacements while the SSTs will be only built in CTA-South array. Improvements in sensitivity and angular resolution compared to other IACTs and space-based telescopes for γ rays are expected for CTA (see Figure 41). Futhermore, the fact of covering energy ranges up to 300 TeV and also reaching the lowest energies∼20 GeV, will be a milestone when this observatory is in operation. Hence, CTA will give a new perspective of the full sky vision.
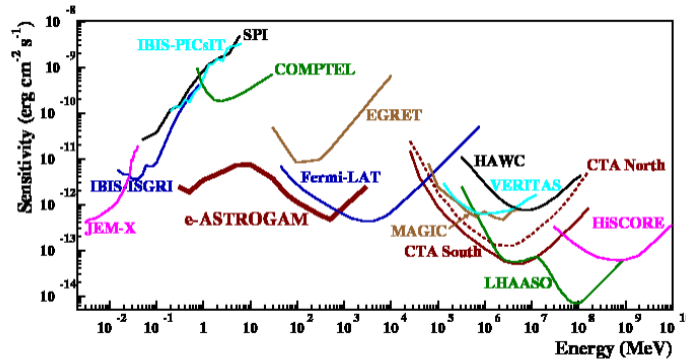

Fig 41. Comparison plot of different telescopes sensitivities, where CTA South and North are also represented in dark red continuous and dotted lines (Elisa Prandini, 2017).

In addition, each type of telescopes (SST, MST and LST) will have also their own purpose working with different sensitivities. One can find out more information about the project and each telescope on the official website of the CTA Observatory.
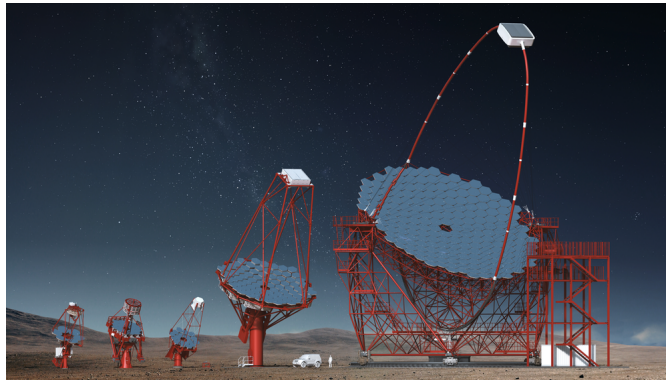

Fig 42. From left to right, three different SST prototype designs, the two MST prototype designs and the LST prototype design. Credit: Gabriel Pérez Diaz, IAC.

With respect to the project status, it is in the current phase of Pre-construction. The first LST telescope is currently under construction on the North Site (La Palma). It will be inaugurated in October 2018, and its conmissioning will start in September 2018. Finally, if all goes as expected, the phase of Pre-Production will take place probably between 2019 and 2021.
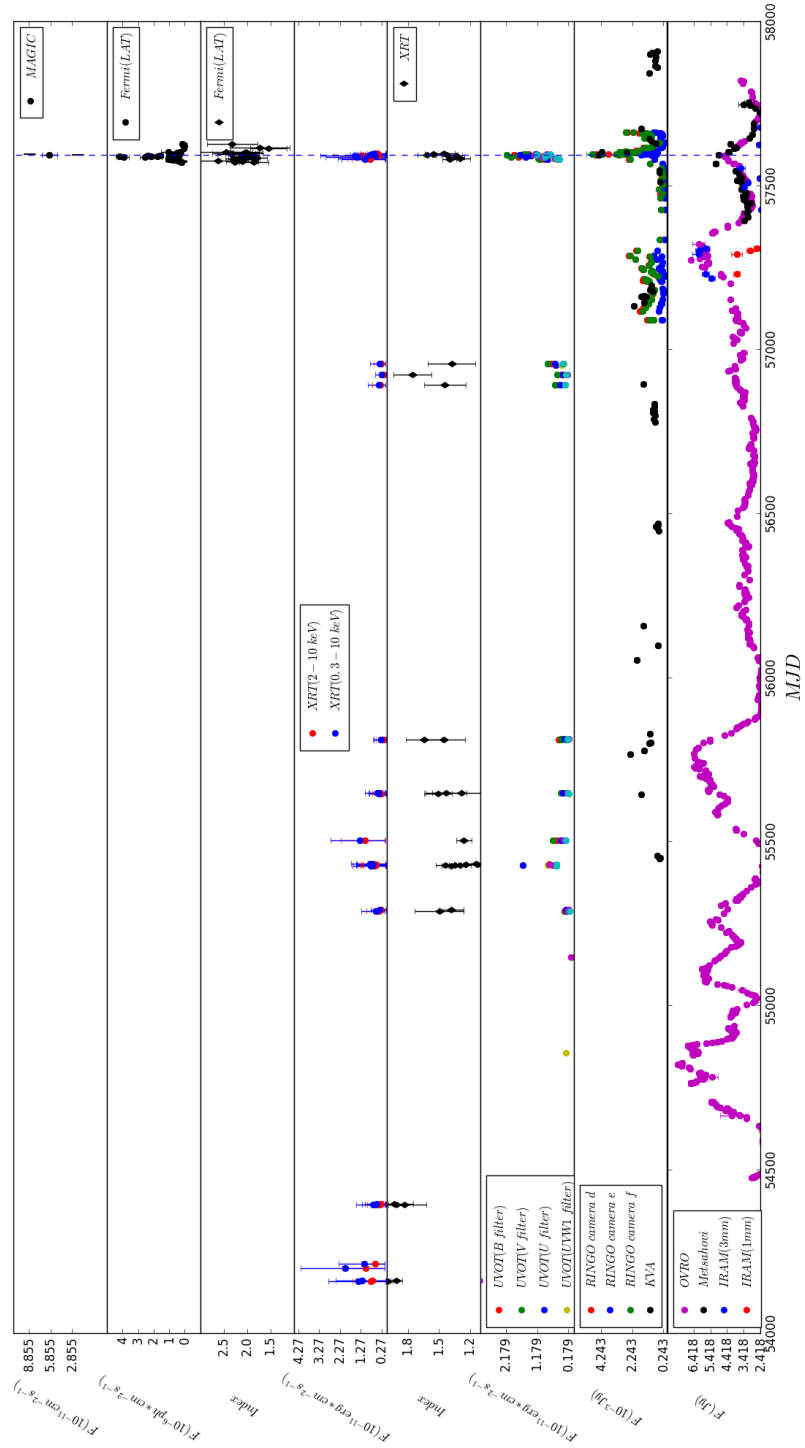
Appendix A

Fig A1. Light curve of OT 081, from radio up to the VHE range. The third and fifth panels represent the photon index derived from the LAT and Swift data, respectively. The dashed blue line represents the time when the flare was observed by MAGIC, on the 25th of July 2016.

Acknowledgements

References

[1] J. Albert, E. Aliu, H. Anderhub, P. Antoranz, A. Armada, C. Baixeras, J. A. Barrio, H. Bartko, D. Bastieri, J. K. Becker, W. Bednarek, K. Berger, C. Bigongiari, A. Biland, R. K. Bock, P. Bordas, V. Bosch-Ramon, T. Bretz, I. Britvitch, M. Camara, E. Carmona, A. Chilingarian, J. A. Coarasa, S. Commichau, J. L. Contreras, J. Cortina, M. T. Costado, V. Curtef, V. Danielyan, F. Dazzi, A. De Angelis, C. Delgado, R. de los Reyes, B. De Lotto, E. Domingo-Santamaría, D. Dorner, M. Doro, M. Errando, M. Fagiolini, D. Ferenc, E. Fernández, R. Firpo, J. Flix, M. V. Fonseca, L. Font, M. Fuchs, N. Galante, R. García-López, M. Garczarczyk, M. Gaug, M. Giller, F. Goebel, D. Hakobyan, M. Hayashida, T. Hengstebeck, A. Herrero, D. Höhne, J. Hose, C. C. Hsu, P. Jacon, T. Jogler, R. Kosyra, D. Kranich, R. Kritzer, A. Laille, E. Lindfors, S. Lombardi, F. Longo, J. López, M. López, E. Lorenz, P. Majumdar, G. Maneva, K. Mannheim, O. Mansutti, M. Mariotti, M. Martínez, D. Mazin, C. Merck, M. Meucci, M. Meyer, J. M. Miranda, R. Mirzoyan, S. Mizobuchi, A. Moralejo, K. Nilsson, J. Ninkovic, E. Oña-Wilhelmi, N. Otte, I. Oya, D. Paneque, M. Panniello, R. Paoletti, J. M. Paredes, M. Pasanen, D. Pascoli, F. Pauss, R. Pegna, M. Persic, L. Peruzzo, A. Piccioli, M. Poller, E. Prandini, N. Puchades, A. Raymers, W. Rhode, M. Ribó, J. Rico, M. Rissi, A. Robert, S. Rügamer, A. Saggion, A. Sánchez, P. Sartori, V. Scalzotto, V. Scapin, R. Schmitt, T. Schweizer, M. Shayduk, K. Shinozaki, S. N. Shore, N. Sidro, A. Sillanpää, D. Sobczynska, A. Stamerra, L. S. Stark, L. Takalo, P. Temnikov, D. Tescaro, M. Teshima, N. Tonello, D. F. Torres, N. Turini, H. Vankov, V. Vitale, R. M. Wagner, T. Wibig, W. Wittek, F. Zandanel, R. Zanin, and J. Zapatero. Discovery of Very High Energy γ-Ray Emission from the Low-Frequency-peaked BL Lacertae Object BL Lacertae. *The Astrophysical Journal*, 666:L17–L20, September 2007.

[2] U. Barres de Almeida and E. M. de Gouveia Dal Pino. Cherenkov Telescope Array (CTA). In *Revista Mexicana de Astronomia y Astrofisica Conference Series*, volume 44 of *Revista Mexicana de Astronomia y Astrofisica, vol. 27*, pages 122–122, October 2014.

[3] Cherenkov Telescope Array (CTA). https://www.cta-observatory.org. 2018.

[4] ETH Institute for Particle Physics. http://ihp-lx.ethz.ch/Stamet/magic/parameters.htmlShapeParameters. 2018.

[5] V. Fallah Ramazani, E. Lindfors, and K. Nilsson. Empirical multi-wavelength prediction method

for very high energy gamma-ray emitting BL Lacertae objects. *Astronomy and Astrophysics*, 608:A68, December 2017.

[6] R. Falomo, M. Bersanelli, P. Bouchet, and E. G. Tanzi. The optical to near-infrared emission of BL Lac objects - Simultaneous observations. *The Astrophysical Journal*, 106:11–27, July 1993.

[7] R. Falomo, R. Scarpa, and M. Bersanelli. Optical spectrophotometry of blazars. *The Astrophysical Journal Supplement Series*, 93:125–143, July 1994.

[8] J. H. Fan and R. G. Lin. Infrared Variation of Radio-selected BL Lacertae Objects. *The Astrophysical Journal Supplement Series*, 121:131–157, March 1999.

[9] A. L. Fey, A. W. Clegg, and R. L. Fiedler. VLBI Observations of Eight Extreme Scattering Event Sources: Milliarcsecond-Scale Structure. *The Astrophysical Journal*, 468:543, September 1996.

[10] J. D. Finke. Compton Dominance and the Blazar Sequence. *The Astrophysical Journal*, 763:134, February 2013.

[11] P. Fortin, S. Fegan, D. Horan, D. Sanchez, Fermi LAT Collaboration, B. Gielbels, Y. Becherini, G. Dubus, M. de Naurois, M. Punch, M. Raue, and H.E.S.S. Collaboration. Gamma-ray emission from AP Librae (PKS1514-241). In *25th Texas Symposium on Relativistic Astrophysics*, page 199, 2010.

[12] D. C. Gabuzda, A. B. Pushkarev, and T. V. Cawthorne. The lambda=6cm VLBI polarization structure of nine BL Lacertae objects. *Monthly Notices of the Royal Astronomical Society*, 307:725–736, August 1999.

[13] G. Ghisellini, C. Righi, L. Costamante, and F. Tavecchio. The Fermi blazar sequence. *Monthly Notices of the Royal Astronomical Society*, 469:255–266, July 2017.

[14] Josefa Becerra González. *Study of very high energy gamma ray sources: discovery of the blazars PKS 1222+ 21 and 1ES 1215+ 303*. PhD thesis, Universidad de La Laguna, 2011.

[15] H.E.S.S. Collaboration, A. Abramowski, F. Aharonian, F. Ait Benkhali, A. G. Akhperjanian, E. Angüner, G. Anton, M. Backes, S. Balenderan, A. Balzer, and et al. The high-energy γ-ray emission of AP Librae. *Astronomy and Astrophysics*, 573:A31, January 2015.

[16] T. Hovatta, H. J. Lehto, and M. Tornikoski. Wavelet analysis of a large sample of AGN at high radio frequencies. *Astronomy and Astrophysics*, 488:897–903, September 2008.

[17] M. Lopez, N. Otte, M. Rissi, T. Schweizer, M. Shayduk, S. Klepser, and for the MAGIC Collaboration. Detection of the crab pulsar with MAGIC. *ArXiv e-prints*, July 2009.

[18] Alicia López Oramas. *Multi-year campaign of the gamma-ray binary LS I+61º 303 and search for VHE emission from gamma-ray binary candidates with the MAGIC telescopes*. PhD thesis, 2014.

[19] MAGIC Collaboration, M. L. Ahnen, S. Ansoldi, L. A. Antonelli, C. Arcaro, D. Baack, A. Babić, B. Banerjee, P. Bangale, U. Barres de Almeida, J. A. Barrio, W. Bednarek, E. Bernardini, R. C.

Berse, A. Berti, W. Bhattacharyya, A. Biland, O. Blanch, G. Bonnoli, R. Carosi, A. Carosi, G. Ceribella, A. Chatterjee, S. M. Colak, P. Colin, E. Colombo, J. L. Contreras, J. Cortina, S. Covino, P. Cumani, P. Da Vela, F. Dazzi, A. De Angelis, B. De Lotto, M. Delfino, J. Delgado, F. Di Pierro, A. Domínguez, D. Dominis Prester, D. Dorner, M. Doro, S. Einecke, D. Elsaesser, V. Fallah Ramazani, A. Fernández-Barral, D. Fidalgo, M. V. Fonseca, L. Font, C. Fruck, D. Galindo, R. J. García López, M. Garczarczyk, M. Gaug, P. Giammaria, N. Godinović, D. Gora, D. Guberman, D. Hadasch, A. Hahn, T. Hassan, M. Hayashida, J. Herrera, J. Hose, D. Hrupec, K. Ishio, Y. Konno, H. Kubo, J. Kushida, D. Kuvež dić, D. Lelas, E. Lindfors, S. Lombardi, F. Longo, M. López, C. Maggio, P. Majumdar, M. Makariev, G. Maneva, M. Manganaro, K. Mannheim, L. Maraschi, M. Mariotti, M. Martínez, S. Masuda, D. Mazin, K. Mielke, M. Minev, J. M. Miranda, R. Mirzoyan, A. Moralejo, V. Moreno, E. Moretti, T. Nagayoshi, V. Neustroev, A. Niedzwiecki, M. Nievas Rosillo, C. Nigro, K. Nilsson, D. Ninci, K. Nishijima, K. Noda, L. Nogués, S. Paiano, J. Palacio, D. Paneque, R. Paoletti, J. M. Paredes, G. Pedaletti, M. Peresano, M. Persic, P. G. Prada Moroni, E. Prandini, I. Puljak, J. R. Garcia, I. Reichardt, W. Rhode, M. Ribó, J. Rico, C. Righi, A. Rugliancich, T. Saito, K. Satalecka, T. Schweizer, J. Sitarek, I. Šnidarić, D. Sobczynska, A. Stamerra, M. Strzys, T. Surić, M. Takahashi, L. Takalo, F. Tavecchio, P. Temnikov, T. Terzić, M. Teshima, N. Torres-Albà, A. Treves, S. Tsujimoto, G. Vanzo, M. Vazquez Acosta, I. Vovk, J. E. Ward, M. Will, D. Zarić, J. Becerra González, Y. Tanaka, R. Ojha, J. Finke, A. Lähteenmäki, E. Järvelä, M. Tornikoski, V. Ramakrishnan, T. Hovatta, S. G. Jorstad, A. P. Marscher, V. M. Larionov, G. A. Borman, T. S. Grishina, E. N. Kopatskaya, L. V. Larionova, D. A. Morozova, S. S. Savchenko, Y. V. Troitskaya, I. S. Troitsky, A. A. Vasilyev, I. Agudo, S. N. Molina, C. Casadio, M. Gurwell, M. I. Carnerero, C. Protasio, and J. A Acosta Pulido. The detection of the blazar S4 0954+65 at very-high-energy with the MAGIC telescopes during an exceptionally high optical state. *ArXiv e-prints*, January 2018.

[20] E. J. Marchesini, I. Andruchow, S. A. Cellone, J. A. Combi, L. Zibecchi, J. Martí, G. E. Romero, A. J. Muñoz-Arjonilla, P. Luque-Escamilla, and J. R. Sánchez-Sutil. Optical flux behaviour of a sample of Fermi blazars. *Astronomy and Astrophysics*, 591:A21, June 2016.

[21] NASA/IPAC Extragalactic Database. https://ned.ipac.caltech.edu. 2018.

[22] National Aeronautics and Space Administration (NASA). https://fermi.gsfc.nasa.gov/ssc/data/analysis/scitools/likeli

[23] National Aeronautics and Space Administration (NASA). https://heasarc.gsfc.nasa.gov/cgi-bin/Tools/xTime/xTime.pl. 2018.

[24] National Aeronautics and Space Administration (NASA). https://www.nasa.gov/content/goddard/fermi-spacecraft-and-instruments. 2018.

[25] A. Nepomuk Otte and Veritas Collaboration. First Detection of a Pulsar above 100 GeV. In *Journal of Physics Conference Series*, volume 375 of *Journal of Physics Conference Series*, page 052023, July 2012.

[26] M. Persic and A. De Angelis. VHE astrophysics: recent developments. *Mem. Societa Astronomica Italiana*, 78:787, 2007.

[27] E. Prandini. Highlights from TeV Extragalactic Sources. *ArXiv e-prints*, June 2017.

[28] T. A. Rector and J. T. Stocke. The Properties of the Radio-Selected 1 Jy Sample of BL Lacertae Objects. *The Astronomical Journal*, 122:565–584, August 2001.

[29] D. Sanchez, B. Giebels, and P. Fortin. The challenging SED of AP Librae. In R. J. Tuffs and C. C. Popescu, editors, *The Spectral Energy Distribution of Galaxies - SED 2011*, volume 284 of *IAU Symposium*, pages 411–413, August 2012.

[30] SSDC Sky Explorer | SED Builder tool. https://tools.ssdc.asi.it. 2018.

[31] M. Stickel, J. W. Fried, and H. Kuehr. The redshifts of the BL Lac objects 1749+096 and 2254+074. *Astronomy and Astrophysics*, 191:L16–L18, February 1988.

[32] M. Stickel, J. W. Fried, and H. Kuehr. The complete sample of 1 Jy BL Lac objects. II - Observational data. *Astronomy and Astrophysics Supplement Series*, 98:393–442, May 1993.

[33] TevCat. http://tevcat.uchicago.edu. 2018.

[34] The Astronomer's Telegram. http://www.astronomerstelegram.org. 2018.

[35] The Fermi Large Area Telescope. http://www-glast.stanford.edu/instrument.html. 2018.

[36] The MAGIC Telescopes. https://magic.mpp.mpg.de. 2018.

[37] I. Torniainen, M. Tornikoski, H. Teräsranta, M. F. Aller, and H. D. Aller. Long term variability of gigahertz-peaked spectrum sources and candidates. *Astronomy and Astrophysics*, 435:839–856, June 2005.

[38] M. Tornikoski, E. Valtaoja, H. Terasranta, A. G. Smith, A. D. Nair, S. D. Clements, and R. J. Leacock. Correlated radio and optical variations in a sample of active galactic nuclei. *Astronomy and Astrophysics*, 289:673–710, September 1994.

[39] UKSSDC | XRT threads. http://www.swift.ac.uk/analysis/xrt. 2018.

[40] University of Durham. https://www.dur.ac.uk/cfai/vhegammaraygroup/physics/groundbased. 2018.

[41] University of Nova Gorica - Center for Astrophysics and Cosmology. http://www.ung.si/en/research/cac/projects/fermi-lat. 2018.

[42] UTAH Department of Physics and Astronomy. https://www.physics.utah.edu/ whanlon/spectrum.html. 2018.

[43] R. Wurtz, J. T. Stocke, and H. K. C. Yee. The Canada-France-Hawaii Telescope Imaging Survey of BL Lacertae Objects. I. Properties of the Host Galaxies. *The Astrophysical Journal Supplement Series*, 103:109, March 1996.